Please cite the following article as:

Flynn, M., Singh, M., Bharath, K., & Sheikhi, S. (n.d.). Effect of fissure drainage on dispersive mixing in porous media gravity currents: an experimental investigation. *InterPore Journal*. Advance online publication. https://doi.org/10.69631/b5x6xn52

Received: 11 Mar. 2025
Accepted: 31 Oct. 2025
Published online (accepted version): 18 Mar. 2026

Effect of fissure drainage on dispersive mixing in porous media gravity currents: an experimental investigation

Mansimran Singh[a], Saeed Sheikhi[a], K. S. Bharath[a], M. R. Flynn[a,*]

[a]*Dept. of Mechanical Engineering, U. Alberta, Edmonton, AB, Canada, T6G 1H9*

Abstract

The prospect of storing hydrogen in depleted natural gas reservoirs requires that the dispersive mixing between injected hydrogen and the cushion gas resident within the porous medium be well understood. Motivated by this observation, we report upon a series of similitude laboratory experiments employing salt and fresh water; experiments use optical techniques to characterize the dispersive mixing that results from porous media gravity current flow. Importantly, the gravity current is supposed to propagate over a "leaky" boundary, i.e. one containing an isolated fissure that allows drainage into an underlying (and dynamically-isolated) layer. Thus do we find that drainage and dispersion are connected: as more (relatively undiluted) fluid drains through the fissure, the remaining gravity current fluid is disproportionately comprised of fluid that has been significantly diluted through dispersive mixing. A novel metric for comparing the relative amount of dispersed fluid present is proposed. We then characterize the variation of this so-called dispersed buoyancy fraction with the gravity current density and source height, the dip angle and the fissure geometry. Thus do we find, for example, that dispersion increases sharply for down-dip flow whereas dispersion may plateau as the fissure area is increased. Select experimental data are contrasted against the predictions of a previously-published theoretical model. The implications of said comparison are then discussed e.g. in the context of model refinement.

Keywords: Dispersion, Gravity current in porous media, Underground hydrogen storage (UHS)

*Corresponding author (mrflynn@ualberta.ca, ORCID 0000-0002-7559-9463)

1. Introduction

The quest for affordable, sustainable energy sources has intensified in recent years, as the detrimental impact of atmospheric carbon emissions has become increasingly evident. Among the potential substitutes for hydrocarbon-based fuels, hydrogen stands out due to its high energy density (on a per unit mass basis) and its ability to contribute to many different components of the energy value chain – see e.g. figure 1 of Hematpur et al. [15]; see also Dunn [8]. While the motivation to generate hydrogen via electrolysis using renewable sources such as wind and solar is clear and compelling, supply inconsistencies necessitate the construction of facilities to store hydrogen for durations ranging from days to years [31]. Short-term storage can be handled easily using pressurized tanks and related surface infrastructure, however, long-term storage of large volumes of hydrogen requires the injection and subsequent withdrawal of compressed gas into geological formations. Indeed, underground hydrogen storage (UHS) offers enormous storage potential, i.e. in the range of 100 GWh according to the predictions of Tarkowski [30]. Realizing this potential requires exploiting various UHS facilities including abandoned mines [5, 20], lined rock [18] or salt caverns [22, 13, 15], aquifers [10, 27] and depleted oil and natural gas reservoirs [1, 12, 9, 19]. Although salt cavern storage offers numerous benefits (e.g. a comparatively sterile environment and minimal hydrogen loss by diffusion), thick halite beds have a geographical distribution described as "limited" [15]. Much more plentiful are aquifers and depleted oil and gas reservoirs and, indeed, these formations typically offer the greatest storage capacity. In either case, however, storage security may be complicated by, among other factors, mixing between compressed hydrogen and "cushion gas," the gas (e.g. CO_2 or N_2) left in formation to maintain operational pressure and to separate hydrogen from water [9, 29, 28, 3].

For hydrogen plumes that propagate laterally under the influence of buoyancy, the mixing described at the end of the last paragraph is expected to be predominately dispersive in nature. As such, Heinemann et al. [14] predicted that the mixing would be enhanced by reservoir heterogeneities. This prediction was verified and quantified by the similitude laboratory experiments of Sahu & Neufeld [26] who studied buoyancy-driven flow through

a medium consisting of stacked horizontal layers of different permeability. As illustrated schematically in their figure 1, flow focusing through high permeability layers causes the vertical density gradient to become unstable leading the formation of convective fingers oriented perpendicular to the permeability jump (see also figure 7 of Huppert et al. [17]). Finger elongation is associated with rapid mixing in the vertical direction and a thickening of the gravity current so that it can no longer be considered long and thin.

Herein, we tackle a problem complementary to Sahu & Neufeld [26]. More precisely, we return to a homogeneous porous medium but impose local rather than distributed drainage for the gravity current that propagates through this medium. In turn, drained fluid shall, after exiting the fissure, flow into a deep layer so that its subsequent flow evolution becomes disconnected from that of the original gravity current and vice-versa. Stated differently, the gravity currents examined in our work never lose their long and thin character. By experiencing localized drainage, however, their forward advance is significantly retarded and the gravity currents therefore become more susceptible to dispersive mixing. Quantifying this connection between drainage and dispersion for different source conditions, fissure areas and dip angles represents the central objective of this work. In order to realize this objective, we perform a series of similitude laboratory experiments using analogue fluids, i.e. salt water as the injectate and fresh water as the ambient. Relative to real geological flows, therefore, the injectate density is larger than, rather than smaller than, that of the fluid saturating the porous medium. Such differences matter little insofar as the dynamical evolution of the flow, i.e. analogous similitude laboratory measurements would be obtained if the injectate was comparatively buoyant rather than dense. This equivalence notwithstanding, we emphasize that our study does not attempt to resolve the complicated dynamics associated with real UHS flows as neatly highlighted, for example, by figure 2 of Heinneman et al. [14]. Rather, our objective is to provide novel insights into dispersive mixing vis-à-vis "leaky" gravity current flow. In the long term, these insights may loosely inform estimates of hydrogen-cushion gas mixing (and, by extension, the economic viability of UHS projects). However, their more likely impact may be to motivate additional targeted UHS studies in the style of Feldmann et al. [9] in which dispersive mixing is considered as one of many complicating

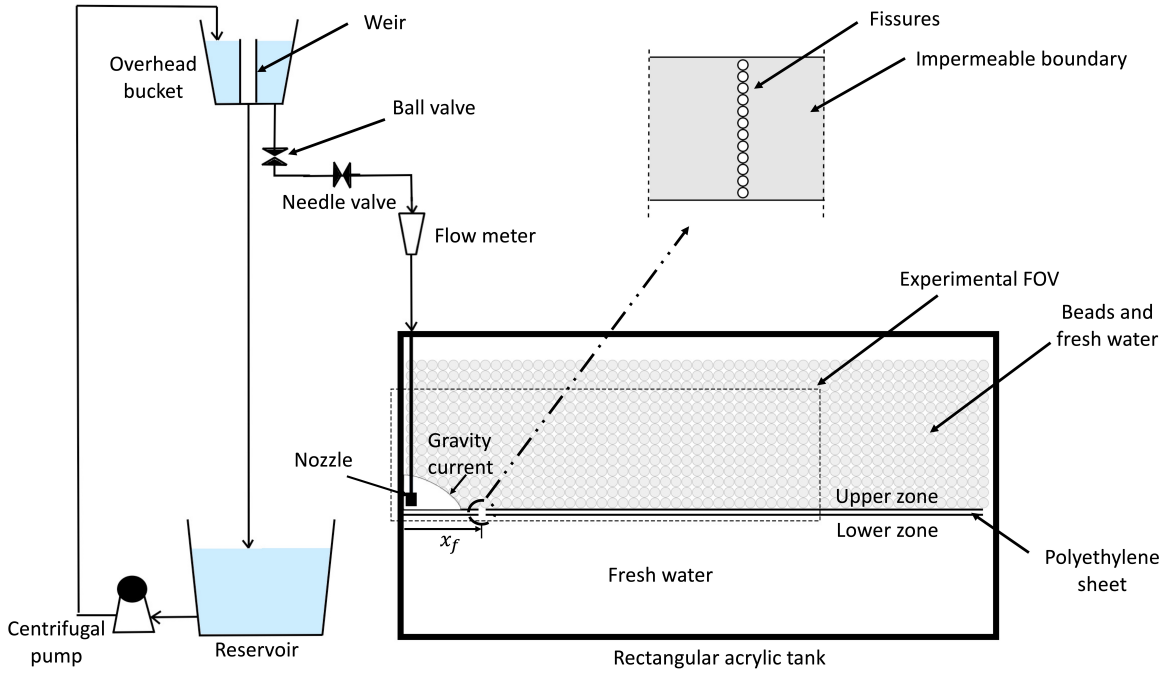

Figure 1: Schematic of the experimental setup. The inset (plan-view) schematic shows the 12 evenly-spaced holes comprising our fissure. The holes in question span the width of the polyethylene sheet. Note that the maximum number of open holes in a given experiment was $\mathcal{N} = 10$.

factors in characterizing the cyclic injection, spreading, drainage and recovery of hydrogen from depleted natural gas reservoirs.

The rest of the manuscript is organized as follows: in section 2, we describe the laboratory set-up and the process applied for capturing experimental images. Then, in section 3, we define the key variables that are relevant to the later analysis of these experimental images. The image processing methodology is explained in section 4 and qualitative and quantitative results are presented in sections 5 and 6, respectively. Section 7 extends the analysis of section 6 by comparing measuring data against the predictions of an analogue theoretical model. Finally, section 8 presents a series of conclusions for the work as a whole.

2. Materials and methods

2.1. Experimental set-up

Experiments were conducted under ambient conditions within a transparent acrylic tank, measuring 118 cm in length, 7.6 cm in width, and 60 cm in depth– see figure 1. Relative to its bottom boundary, the tank was filled over the approximate depth range $z = 16\,\text{cm}$ to $z = 40\,\text{cm}$ with a random distribution of $3.0\,\text{mm} \pm 0.2\,\text{mm}$ diameter glass beads. After adding the beads, the tank was then filled over its entire depth with tap water of density, $\rho_a = 0.998\,\text{g/cm}^3$. According to information provided by the manufacturer, the bead density was $1.54\,\text{g/cm}^3$, large enough that the bead pack did not deform under the influence of fluid flow.

The tank was divided into upper vs. lower zones using an opaque 1/4-inch polyethylene sheet that extended 115 cm longitudinally. To isolate one zone from the other and prevent unwanted leaks of dense gravity current fluid, 1/8-inch gasket tape was added to the edges of the polyethylene sheet. In turn, the polyethylene sheet was supported by five, 15 cm tall 3-D printed polyvinyl chloride (PVC) I-beams to ensure stability. The I-beam spacing and polyethylene rigidity were such that the sheet exhibited minimal deformations, i.e. the bottom boundary of the flow domain can be considered flat.

Although the polyethylene sheet and perimetric gasket formed an otherwise impermeable barrier, we drilled a total of 12 evenly-spaced holes across the sheet width where each hole diameter measured 3.175 mm – see the inset image to figure 1. The openings in question were arranged in a line and were situated 15 cm from the left boundary of the tank. Meanwhile, and on the right-hand side of the tank, a gap of approximately 3 cm was left between the polyethylene sheet edge and the inside tank wall. This gap, which was covered with a stiff mesh to prevent a collapse of the bead pack, provided a passageway for ambient fluid to flow from the lower zone to the upper zone. Such a flow was a necessary consequence of drainage through the fissure, i.e. the 3 cm gap insured that the fissure flow was unidirectional and downward. In turn, drainage was unimpeded by obstacles to the flow path from the lower zone because the lower zone was devoid of glass beads. In the upper zone, by contrast, the

bead layer was approximately 24 cm thick. We estimated the medium permeability, k, using the semi-empirical relationship proposed by Kozeny and Carman and further described by Dullien [7], i.e.

$$k = \frac{d^2\phi^3}{180(1-\phi)^2} \tag{1}$$

Here d is the bead diameter and ϕ is the porosity. Consistent with the random packing arrangement of the (spherical) glass beads, we set $\phi = 0.38$ [11].

As illustrated schematically in figure 1, dense gravity current fluid was injected into the tank using a 3-D printed nozzle, which was situated in the left-most corner of the upper zone. Depending on the specific experimental setup, the nozzle was either aligned flush with the impermeable boundary, as shown in figure 1, or else elevated. In this latter configuration, injected fluid fell some nontrivial vertical distance before striking the polyethylene sheet thereby accelerating and entraining ambient fluid during its descent. The nozzle discharge area measured 2.8 cm^2 and its length measured 6.45 cm such that it very nearly spanned the inside width of the tank. Moreover, and as described in more detail in Roes [23], the nozzle was designed to minimize the source momentum flux and to discharge a uniform flow along its length, even at low flow rates. Nozzle source fluid (i.e. the injectate) consisted of a saline solution to which Procion MX Navy dye was added for flow visualization purposes. In a typical experiment, the dye concentration measured 0.04 g per 1 L of tap water where the mass of dye powder was measured using a Fisher Scientific Education SLF303 balance. At such small concentrations, the dye had a negligible impact on the solution density, which was instead fixed by the addition of crystalline salt (NaCl). Solution densities were measured using an Abbemat 3000 refractometer programmed to output fluid density based on an internal measurement of the index of refraction for salt water.

Saline fluid was supplied to the nozzle using the set-up illustrated schematically on the left-hand side of figure 1. Dyed, saltwater solutions were made in 22 L batches in the floor-level reservoir. By connecting this reservoir to a centrifugal pump (Little Gaint Pump Co., Model 3-MD), saline fluid was added to an overhead bucket containing an internal cylindrical weir. This weir maintained a constant water level (and therefore constant nozzle

supply pressure) over the course of a particular experiment. As shown in figure 1, saline fluid flowing over the weir was returned to the reservoir whereas a separate saline fluid stream flowed to the nozzle and was thereafter dischared in the form of a dense gravity current. Along the way, this latter stream of saline fluid flowed through plastic tubing (inner diameter of 12.7 mm) that connected the overhead bucket to a plastic on/off ball valve, a flow control needle valve (Swagelock, SS-8GUF8) and a Gilmont GV-2119-S-P analogue flow meter. Using this set-up, saline fluid flow rates of 1.0 mL/s were obtained.

2.2. Image capture and dispersion analysis

Over the course of each experiment, digital images were recorded every 30 s using a Canon Rebel EOS T2i 18.0 MP camera, outfitted with an 18-55 mm IS II zoom lens. The camera featured 5184 $\times$ 3156 pixels and a resolution of 72 dpi. To ensure consistent backlighting, two 3M 1880 overhead projectors were used, both of width were positioned at the vertical midpoint of the tank. One projector was situated between the left tank wall and the vertical mid-plane; the other was situated between the vertical mid-plane and the right tank wall. Both projectors sat 1 m behind the back wall of the tank. Along the outside surface of this back wall, we applied a sheet of tracing paper, which diffused the incoming light and thereby improved both lighting uniformity and image clarity.

Important to reiterate is that our tank width was small and the nozzle supplying dense fluid spanned almost the entire inside width. The resulting flow was therefore approximately 2-D rectilinear. Surely the flow included transverse dispersion, however, by positioning the camera directly in front of the tank, we did not visualize nor measure dispersive mixing across the tank width. Rather, and consistent with e.g. Sahu & Neufeld [26], our focus was on dispersion in the longitudinal (x) and wall-normal (z) directions. In both cases, dispersion may have been locally enhanced at the sidewalls, i.e. due to the well-known increase of porosity at a (vertical) boundary. However, and because our optical method effectively integrated dye concentrations across the entire tank width, sidewall effects were considered to be small.

2.3. Experimental sequence

As summarized in Appendix A, our investigation consisted of a total of 48 experiments where we varied the tank angle of inclination, θ, the number, $\mathcal{N}$ of open holes within the fissure, the source fluid density (as characterized by an Atwood number, At – see equation 6 below) and the nozzle elevation, z_n. Regarding the former parameter, we considered a total of five inclination angles, i.e. $\theta = -5°$, $-2.5°$, $0°$, $2.5°$ and $5°$ where $\theta < 0°$ and $\theta > 0°$ respectively correspond to up- and down-dip gravity current flow. Of these five inclination angles, $\theta = 0°$ proved the most temperamental owing to the difficulty of removing air bubbles from the vicinity of the fissure holes. Because of the impact of such bubbles on injectate drainage, our study of the $\theta = 0°$ case was limited to scenarios where $\mathcal{N} = 0$. For other inclination angles, a greater range of $\mathcal{N}$ was possible, i.e. we considered six different fissure configurations ranging from zero fissure holes open to 10 fissure holes open. We also considered two different source fluid densities, i.e. $\rho_s \simeq 1.01\,\mathrm{g/cm^3}$ and $\rho_s \simeq 1.02\,\mathrm{g/cm^3}$. Finally, we considered nozzle elevations of between 0 cm (signifying a nozzle that abutted the polyethylene sheet) and 10 cm (signifying a nozzle situated at the approximate mid-depth of the bead pack and still oriented normal to the polyethylene sheet).

Underpinning each of our experiments was a series of calibration images, which were collected every time the bead pack and/or inclination angle was changed. These calibration images applied Procion MX Navy dye concentrations measuring 0%, 20%, 40%, 50%, 60%, 80%, 100%, and 120% of the dye concentration of the nozzle source fluid, i.e. the fluid contained within the reservoir of figure 1. The calibration images facilitated the analysis of our experimental snapshots in a manner to be explained in section 4. Before turning to this discussion, it is first necessary to list and discuss some of the key variables germane to our study. Such is the purpose of the following section.

3. Parameter characterization

Consistent with Neufeld et al. [21], we define characteristic horizontal and vertical length scales as

$$L = x_f\,, \qquad \text{and} \qquad H = \left(\frac{x_f \dot{Q}_s \phi \nu}{k g_s' w}\right)^{\frac{1}{2}}\,, \tag{2}$$

respectively, and a characteristic time scale as

$$T = \left(\frac{x_f^3 \phi \nu w}{k g_s' \dot{Q}_s}\right)^{1/2}\,. \tag{3}$$

In (2, 3), x_f is the distance from the upstream inside tank wall to the middle of the fissure – see figure 1. Also, $\dot{Q}_s$ is the source volume flow rate, ν is the water kinematic viscosity, w is the tank width, and g_s' is the reduced gravity, defined in terms of the source and ambient fluid densities as

$$g_s' = g\left(\frac{\rho_s - \rho_a}{\rho_a}\right)\,. \tag{4}$$

Having defined the characteristic length and time scales, we can now non-dimensionalize distances and time via

$$x^* = x/L\,, \qquad z^* = z/H\,, \qquad t^* = t/T\,. \tag{5}$$

The densities ρ_s and ρ_a are necessary for defining the reduced gravity g_s' of (4); they are likewise important in defining an Atwood number, which characterizes the importance of buoyancy. The Atwood number in question is defined as

$$\mathrm{At} = \frac{\rho_s - \rho_a}{\rho_s + \rho_a}\,. \tag{6}$$

A major thrust of our investigation is to estimate, as a function of time, the amount of injected fluid that remains within, vs. drains out of, the porous medium. However, characterizing this amount is subject to context. On the one hand, it may be appropriate to measure the amount of fluid remaining within the porous medium by its volume. Given the approximately 2D nature of the gravity current flow in our narrow tank, we measure this volume on a per unit tank span basis. As such, and by applying the post-processing

algorithms to be discussed in the next section, we calculate the resulting area using one of the following two equations:

$$A_{\text{bulk}} = \int_0^{x_{\text{nose, bulk}}} \int_0^{h_{\text{bulk}}(x)} \mathrm{d}z\, \mathrm{d}x\,, \tag{7}$$

and

$$A_{\text{disp}} = \int_0^{x_{\text{nose, disp}}} \int_{h_{\text{bulk}}(x)}^{h_{\text{disp}}(x)} \mathrm{d}z\, \mathrm{d}x\,, \tag{8}$$

where the dimensional (and time-dependent) variables $x_{\text{nose,bulk}}$, $x_{\text{nose,disp}}$, h_{bulk} and h_{disp} are defined in figure 2. Consistent with Bharath et al. [2] and follow-on investigations, (7) and (8) distinguish between the bulk and dispersed phases of the gravity current. As we discuss in greater detail below, bulk fluid has a density comparable to ρ_s, i.e. it remains relatively undiluted by ambient fluid. Conversely, dispersed fluid has a density closer to ρ_a and so is more impacted by dispersive mixing. From (7), A_{bulk} is the area occupied by bulk fluid and is calculated with reference to the depth, h_{bulk}, of bulk fluid measured from the neighborhood of the nozzle to the leading edge (or nose) of the bulk phase where, by definition, $h_{\text{bulk}} \to 0$. Similar comments apply to A_{disp}, which represents the area occupied by the dispersed phase. In evaluating A_{disp} from (8), note that dispersed fluid always separates bulk fluid from ambient fluid such that $x_{\text{nose,disp}} > x_{\text{nose,bulk}}$ and $h_{\text{disp}} > h_{\text{bulk}}$. As shown in figure 2, h_{disp} is the combined depth of the bulk and dispersed phases. Note, furthermore, that the nose positions $x_{\text{nose,bulk}}$ and $x_{\text{nose,disp}}$ are both measured from the upstream interior wall of the tank.

Finally, the areas defined by (7) and (8) may be rendered non-dimensional via

$$A_{\text{j}}^{*} = \frac{\phi A_{\text{j}} w}{\dot{Q}_s T}\,, \tag{9}$$

where the subscript j stands for 'bulk' or 'disp.'

In other contexts, it may be more appropriate to measure the amount of source fluid remaining within the porous medium not by its volume per unit span but rather by its buoyancy per unit span, B. By this metric, the key parameters characterizing the bulk- and dispersed-phases are

$$B_{\text{bulk}} = \int_0^{x_{\text{nose, bulk}}} \int_0^{h_{\text{bulk}}(x)} g'\, \mathrm{d}z\, \mathrm{d}x\,, \tag{10}$$

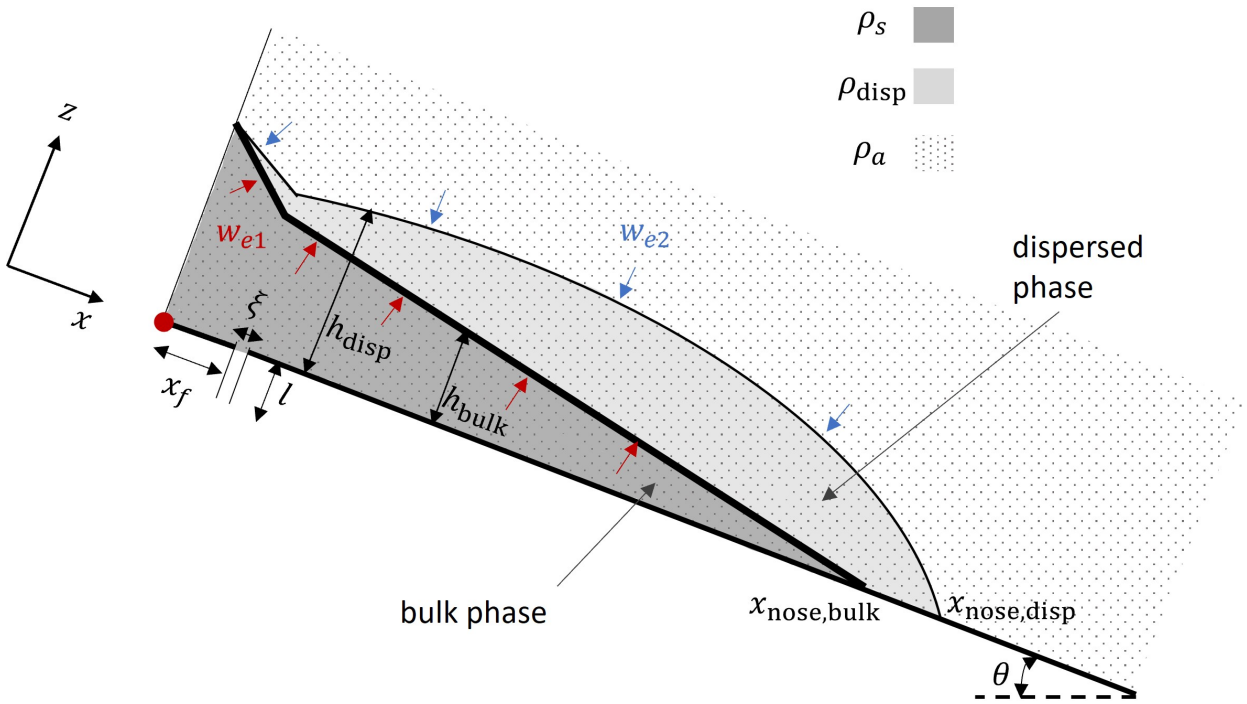

Figure 2: Two-dimensional gravity current flow over an inclined boundary. Both bulk and dispersed phases appear in the gravity current, whose origin is indicated by the red dot. Included in this schematic are variables pertaining to the theoretical model developed in Appendix B, i.e. the entrainment velocities w_{e1} and w_{e2} and the width, ξ, and depth, l, of the (line) fissure. (Figure adapted from figure 1 of Sheikhi et al. [29].)

and

$$B_{\text{disp}} = \int_0^{x_{\text{nose, disp}}} \int_{h_{\text{bulk}}(x)}^{h_{\text{disp}}(x)} g' \, \mathrm{d}z \, \mathrm{d}x \,, \tag{11}$$

respectively. Analogous to (4), $g' \equiv g(\rho - \rho_a)/\rho_a$ where $\rho = \rho(\boldsymbol{x}, t)$ is the fluid density as measured anywhere within the domain. Note, however, that outside of the bulk or dispersed phases, $\rho = \rho_a$ and $B_j = 0$. Also, and similar to (9), we can non-dimensionalize the above variables by defining

$$B_{\text{j}}^* = \frac{\phi B_{\text{j}} w}{\dot{Q}_s g_s' T} \tag{12}$$

In the analysis to follow, we emphasize measures of buoyancy (i.e. B_{bulk} and B_{disp}) rather than of volume (i.e. A_{bulk} and A_{disp}). Consider, for instance, a scenario in which the mixing of bulk fluid results in a dispersed phase that is voluminous but dilute. A_{disp} may equal or

even exceed A_{bulk}, however, a comparison of A_{disp} and A_{bulk} is misleading because most of the solute (i.e. salt and dye) remains in the bulk phase. Comparing B_{disp} and B_{bulk} avoids this confusion because B_{disp} takes into account both the volume occupied by the dispersed fluid and also its solute concentration. By analogy with the UHS example discussed in section 1, losing a proportion of injected hydrogen to dispersive mixing is expected. Of key importance, commercial and otherwise, is whether this fraction is large or small, not whether the gas lost spans a large or small volume within the depleted reservoir.

Motivated by the above discussion, we recognize that the fraction of the total buoyancy that resides in the dispersed phase provides a straightforward means of characterizing the degree of mixing associated with the advance and drainage of the gravity current. The quantity in question can be defined as

$$\overline{B}^{*}_{\mathrm{disp}} = \frac{B_{\mathrm{disp}}}{B_{\mathrm{disp}} + B_{\mathrm{bulk}}}\,. \tag{13}$$

For brevity, we refer to $\overline{B}^{*}_{\mathrm{disp}}$ as the 'dispersed buoyancy fraction.'

4. Image processing

This section outlines the crucial steps taken to distill experimental snapshots into matrices amendable to the analysis to appear in sections 5 and 6. Each of the image processing steps was performed using Matlab.

4.1. Image alignment and conversion

As indicated by table A.2, the vast majority of our experiments inclined the tank through a nonzero angle, θ. Because the camera orientation was fixed and parallel to the ground, images were rotated until the (perpendicular) tank edges appeared as vertical and horizontal in the Matlab figure window. RGB images were then converted to grey scale. Attention then shifted to the region of interest, specifically the area within 15 cm of the polyethylene sheet and 65 cm of the left (upstream) tank wall. However, and due to the presence of the nozzle and its 12.7 mm diameter feeder tubing, the left-most 5 cm of this rectangular region was later cropped. By applying background image subtraction (using, as the reference image,

the very first image from each set, which showed the bead pack before flow initialization), it became easier to visualize field-of-view changes specifically resulting from the forward advance and mixing of the gravity current.

4.2. Image refinement and noise reduction

Given the sensitivity of the experiments e.g. to light intensity variations, further image refinement was applied, i.e. using order-statistic filtering. This process helped to eliminate noise and produce a sharper gradient, enhancing the visual signatures of mixing in each of the false color (i.e. background-subtracted) images. The specific median filter applied operated over a 5×5 pixel area, identifying and replacing low-intensity areas in both calibration and experimental images with the median value of the region in question. By aligning the intensity of a particular pixel with its neighbors, this technique significantly reduced noise e.g. due to light reflection effects. Noise-reduction benefits were apparent both in regions within and outside of the gravity current. In the interests of consistency, we applied the same filtering techniques to all eight calibration images and likewise to each of the experimental images associated with that calibration set. Figure 3 shows the variation of pixel intensity as measured from the top to bottom of a representative experimental image. The noise is substantially reduced in the right-hand side panel, which corresponds to a filtered experimental image.

4.3. Image Calibration (pixel intensity to fluid density)

Within any one of our experimental images, the process of converting pixel intensities to dye concentrations required adherence to a computationally-intensive calibration process. As noted already, each experimental image was analyzed with reference to a series of eight calibration images collected prior to flow initialization. Calibration images were captured over a range of dye intensities (see subsection 2.3) so that at each of the more than two million pixels in a representative experimental image, an eight point calibration curve of pixel intensity vs. dye intensity could be drawn. An example of such a calibration curve is shown in figure 4 where pixel intensities have been normalized such that an intensity value of unity

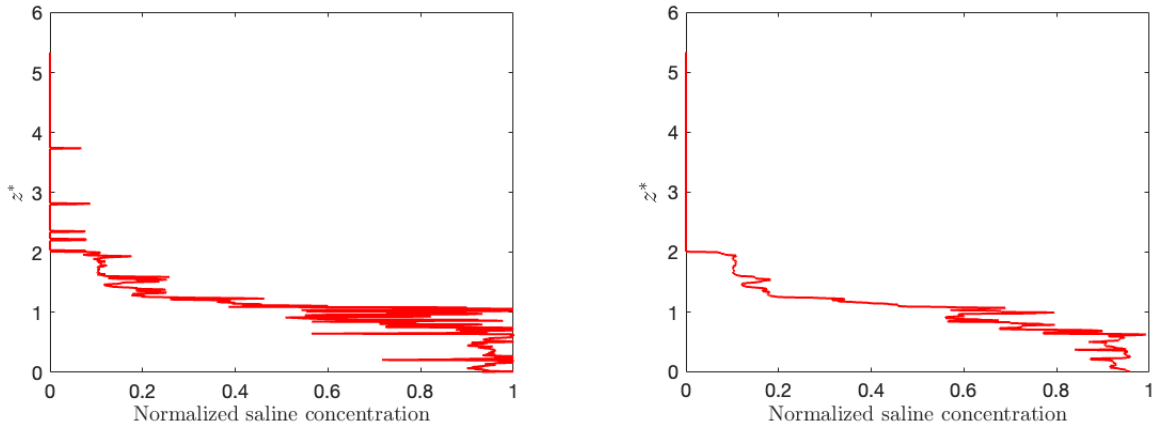

(a) Before order-statistic filtering

(b) After order-statistic filtering

Figure 3: Vertical variation of the normalized pixel intensity, as measured for experiment E1 such that At $= 0.01$, $\theta = 5°$, $z_n^* \equiv z_n/H = 0$ and $\mathcal{N} = 0$ – see table A.2. Profiles are collected 4 cm downstream of the left-hand side of the tank at time $t = 720$ s. The precise meaning of the x-axis variable is explained in subsection 4.3.

corresponds to a Procion MX Navy dye concentration of 0.04 g/L. By applying Matlab's `interp1` and linearly interpolating between the eight points comprising each calibration curve, it was possible, when analyzing laboratory images, to assign a unique dye intensity to each pixel and for every frame within an experimental data set. As with the study of Dong & Salvadurai [6], spatial variations in the bead pack intensity made it essential to construct pixel-specific calibration curves rather than, say, a universal calibration curve to be applied over the entirety of the field of view (FOV).

Of course, dye intensities are of much less interest than, say, fluid densities or solute concentrations. To this end, we exploit the fact that ours is a comparatively large-Péclet number flow such that dye and salt are expected to mix at approximately equal rates. Stated differently, a key assumption of our study is that the dye intensity serves as a direct proxy for the saline concentration. Thus can we straightforwardly convert from a normalized dye concentration to a normalized salt concentration where, consistent with the above discussion, a normalized pixel intensity of unity corresponds to a dye concentration of 0.04 g/L, which corresponds, in turn, to a normalized saline concentration of unity. Indeed, it is this

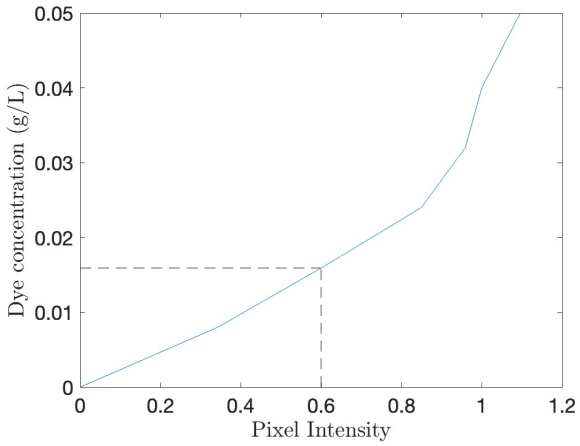

Figure 4: Example calibration curve as constructed for one of the pixels corresponding to experimental images from E1– see table A.2. The dashed black lines illustrate the process of correlating a particular normalized pixel intensity (here 0.6) with a particular dye concentration (here 0.016 g/L).

latter variable that we consider in figure 3. In figure 3, the normalized saline concentration approaches unity towards the bottom of the field of view where gravity current densities most closely match the source density, ρ_s. Above this region of highly concentrated (or 'bulk') fluid is a dispersed region where normalized saline concentrations fall well above zero but well below unity. Characterizing the relative volume and buoyancy of this quantity of dispersed fluid is, of course, a major objective of the present study. Before turning to this topic, however, it is first necessary to distinguish between the bulk and dispersed phases. We discuss this (and other) topics next.

5. Qualitative analysis

By applying the post-processing steps detailed in subsections 4.1 to 4.3, it was possible to generate images such as those presented in the collage of figure 5. Here, we show snapshots collected at three different instants in time corresponding to $t^* = 0.9$ (left column), $t^* = 1.8$ (center column) and $t^* = 2.6$ (right column) where t^* is defined by (5). This trio of images is reproduced six times over where, scanning down the columns of figure 5, the number, $\mathcal{N}$, of open fissure holes increases from zero to 10 in steps of two. All other parameters (i.e. source conditions and angle of inclination) are held fixed such that $\mathrm{At} = 0.01$, $\theta = 5^\circ$

and $z_n^* \equiv z_n/H = 0$. A figure analogous to figure 5 but considering a larger source density, i.e. At $= 0.02$ is shown in figure 6.

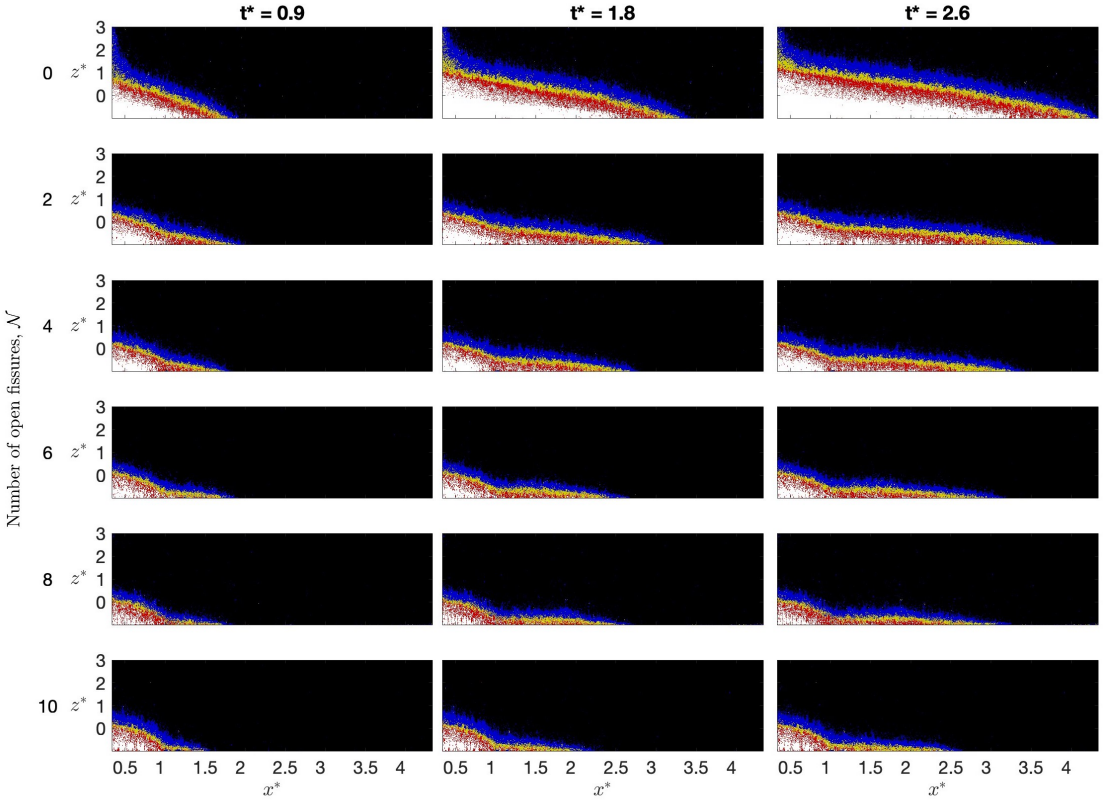

Figure 5: Collage image showing the time evolution of six different experiments (i.e. E1, E5, E9, E13, E17 and E21), each corresponding to a different number of open fissure holes. The spatial coordinates x^* and z^* are defined by (5) where $x^* = 1$ shows the fissure location. Colored shading is applied over the following range of normalized saline concentrations: black – 0 to 0.10; blue – 0.10 to 0.25; yellow – 0.25 to 0.50; red – 0.50 to 0.75; and white – 0.75 to 1.

As noted in the caption to figure 5, the color coding delineates the degree of dispersion realized in each experimental image. Thus white shading appears close to the bottom of the frame in the different panels of figures 5 and 6: immediately above the polyethylene sheet there is limited opportunity for diluting gravity current fluid with ambient fluid – see e.g. figure 3 and the discussion thereof. Above this white region, one observes shades of red, yellow, blue and black corresponding to a progression from fluid whose salinity is relatively

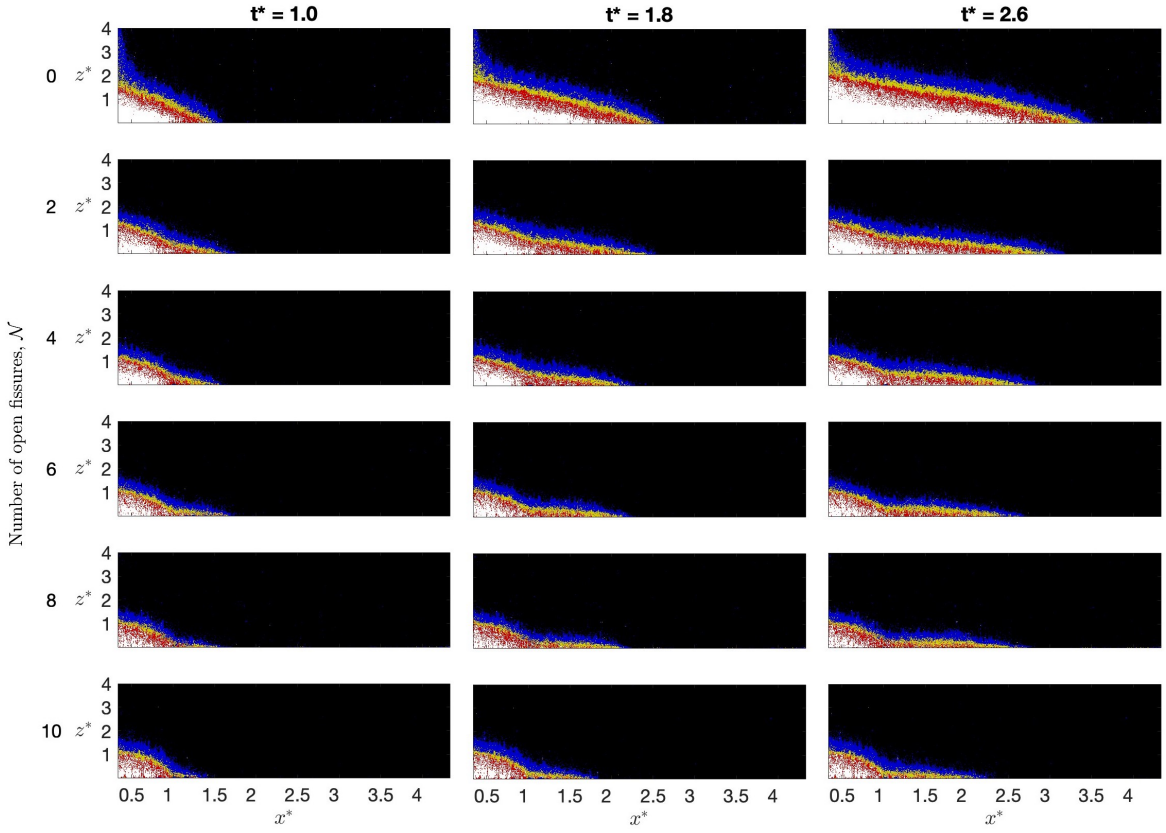

Figure 6: As in figure 5 but considering At = 0.02 and experiments E2, E6, E10, E14, E18 and E22.

close to that of the source vs. that of the ambient.

An interesting aspect of figure 5 is that increasing $\mathcal{N}$ from zero to 10 has only a modest impact on the thickness of the red, yellow and blue regions. However, changing $\mathcal{N}$ has a substantial impact on the volume of fluid draining through the fissure. For instance, when $\mathcal{N} \geq 6$, the white region becomes very small even for t^* as large as 2.6. Correspondingly, and compared to the $\mathcal{N} = 0$ baseline, the gravity current advances much more slowly for large $\mathcal{N}$ with fluid having a density close to that of the source propagating little past $x^* = 1$.

Of course, a slower rate of frontal advance should not be confused with an absence of downstream influence: given sufficient time, gravity current fluid can propagate long down-dip distances, even if $\mathcal{N}$ is comparatively large. This fact is confirmed by figure 7. It considers the same six experiments from figure 5 but shows, as a function of $\mathcal{N}$, the gravity current profile at $t_{x^*=4}$, defined as the point in time where the gravity current front first

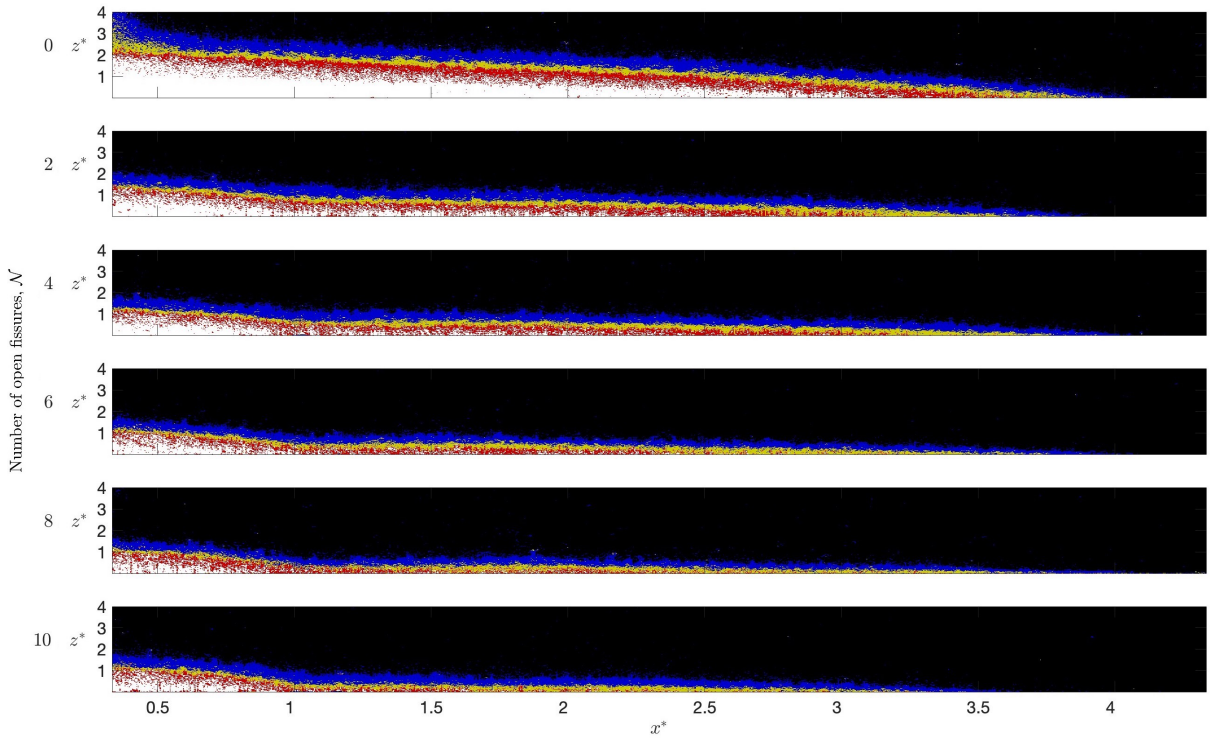

Figure 7: As in figure 5 but showing the longer-term evolution of the flow such that the gravity current nose just overlaps with $x^* = 4$. When $\mathcal{N} = 0$, 2, 4, 6, 8 and 10, $t^*_{x^*=4} = 1.1$, 1.3, 1.6, 1.8, 1.9 and 2.2, respectively.

reaches the downstream location $x^* = 4$. Figure 7 makes clear that the volume of fluid whose saline concentration falls well below ρ_s is, relative to the total volume of gravity current fluid present, substantially larger when $\mathcal{N} = 10$ vs. $\mathcal{N} = 0$. Such is the consequence of having most of the high-density source fluid drain away through the open fissure. In this way, and measured in proportional rather than absolute amounts, draining and dispersion are closely linked with the former serving to increase the relative importance of the latter – c.f. Sheikhi et al. [29] and Sheikhi & Flynn [28].

Given the conclusions from the end of the last paragraph, it is interesting to revisit the differences between figure 5 (At = 0.01) and figure 6 (At = 0.02). When the Atwood number is doubled, draining becomes even more significant such that the gravity currents of figure 6 advance more slowly than their counterparts from figure 5. For $\mathcal{N} \geq 4$, for instance, the region beyond the fissure is practically devoid of fluid having a normalized

saline concentration exceeding 0.75. When draining is especially robust, we lack a sufficient supply of dense gravity current fluid to drive mixing by dispersion. In such large $\mathcal{N}$ cases, the relative significance of the yellow and blue regions will actually be shown to decrease – see e.g. figure 12 a below.

Notwithstanding the colorful variety of concentrations evident in figures 5, 6 and 7, it is more advantageous to now transition to a binary point-of-view where we classify fluid nontrivially contaminated with salt/dye into one of two different categories. To wit, 'bulk' and 'dispersed' fluid will respectively correspond to any fluid having a normalized saline concentration greater than and less than 0.5. In essence, bulk fluid appears as white and red in figures 5, 6 and 7 whereas dispersed fluid appears as yellow and blue. Having established these definitions, we are now well positioned to examine the relative abundance of one vs. the other fluid type as a function of At, θ, z_n^* and $\mathcal{N}$.

6. Quantitative analysis

With reference to the definitions of section 3 and the experiments indicated in figures 5 and 7, figure 8 shows the evolution of A_{j}^* and B_{j}^* for different $\mathcal{N}$. Figures 8 a, b respectively show the time variation of dispersed (equation 8) and bulk area (equation 7). As anticipated, A_{disp}^* increases with time, however, the curves in question exhibit smaller slopes for larger $\mathcal{N}$: the dispersed phase is fed by the bulk phase, so any increase in bulk fluid drainage results in a corresponding decrease in the volume of the dispersed phase. Focusing on figure 8 b, it is evident that A_{bulk}^* exhibits an even greater sensitivity to $\mathcal{N}$ than does A_{disp}^*. Notably, for experiments with $\mathcal{N} = 8$ or 10, A_{bulk}^* plateaus just above 0.2.

From the equations of section 3, we anticipate that B_{disp}^* should be substantially less than A_{disp}^*; a comparison of figures 8 a and c confirms this expectation. The corresponding difference between B_{bulk}^* (figure 8 d) and A_{bulk}^* (figure 8 b) is less extreme because, by definition, bulk fluid has a density much closer to that of the source. In figures 8 b,d, we observe that the baseline $\mathcal{N} = 0$ case represents an outlier where, for example, both A_{bulk}^* and B_{bulk}^* increase rapidly and linearly. By contrast, B_{bulk}^* and B_{disp}^* exhibit anemic growth for large $\mathcal{N}$ in which case B_{bulk}^* plateaus just as with A_{bulk}^*.

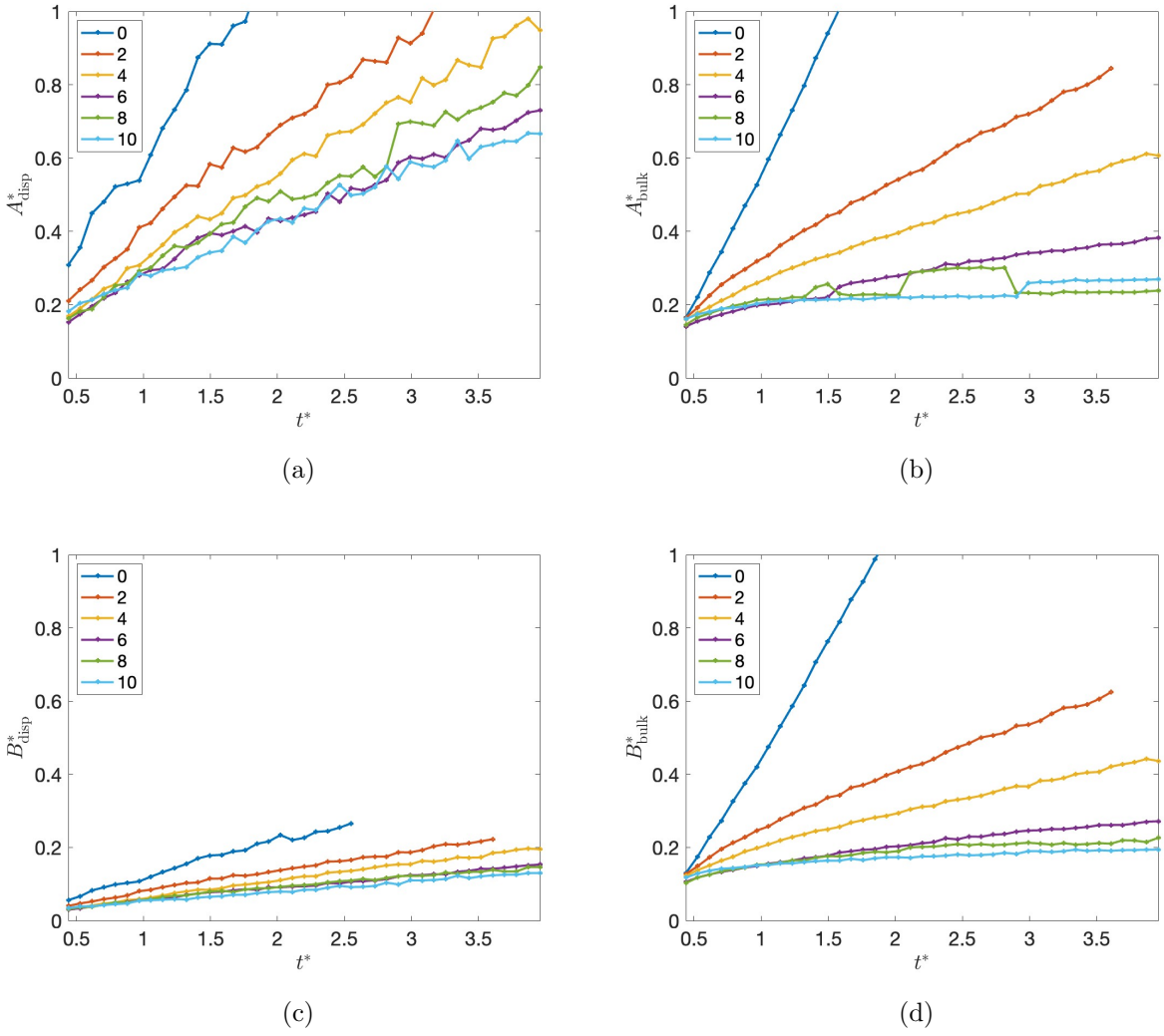

Figure 8: Temporal evolution of the (a) dispersed area fraction, A^*_{disp}, (b) bulk area fraction, A^*_{bulk}, (c) dispersed buoyancy fraction, B^*_{disp} and, (d) bulk buoyancy fraction, B^*_{bulk}. Consistent with figures 5 and 7, At $= 0.01$, $\theta = 5°$, and $z^*_n = 0$. The number, $\mathcal{N}$, of open fissure holes is indicated in the legends.

In this last paragraph, qualitative comparisons are drawn between B^*_{disp} and B^*_{bulk}. The discussion can be made more precise by considering $\overline{B}^*_{\text{disp}}$. According to (13), $\overline{B}^*_{\text{disp}}$ measures the buoyancy of the dispersed phase as a fraction of the overall buoyancy associated with the gravity current. Figure 9 shows $\overline{B}^*_{\text{disp}}$ vs. time and $\mathcal{N}$. Here it is apparent that $\overline{B}^*_{\text{disp}}$ generally increases as the number of open fissure holes is increased. As regards the influence of t^*, the dependence is more nuanced: for $\mathcal{N} \geq 2$, we observe a modest increase of $\overline{B}^*_{\text{disp}}$

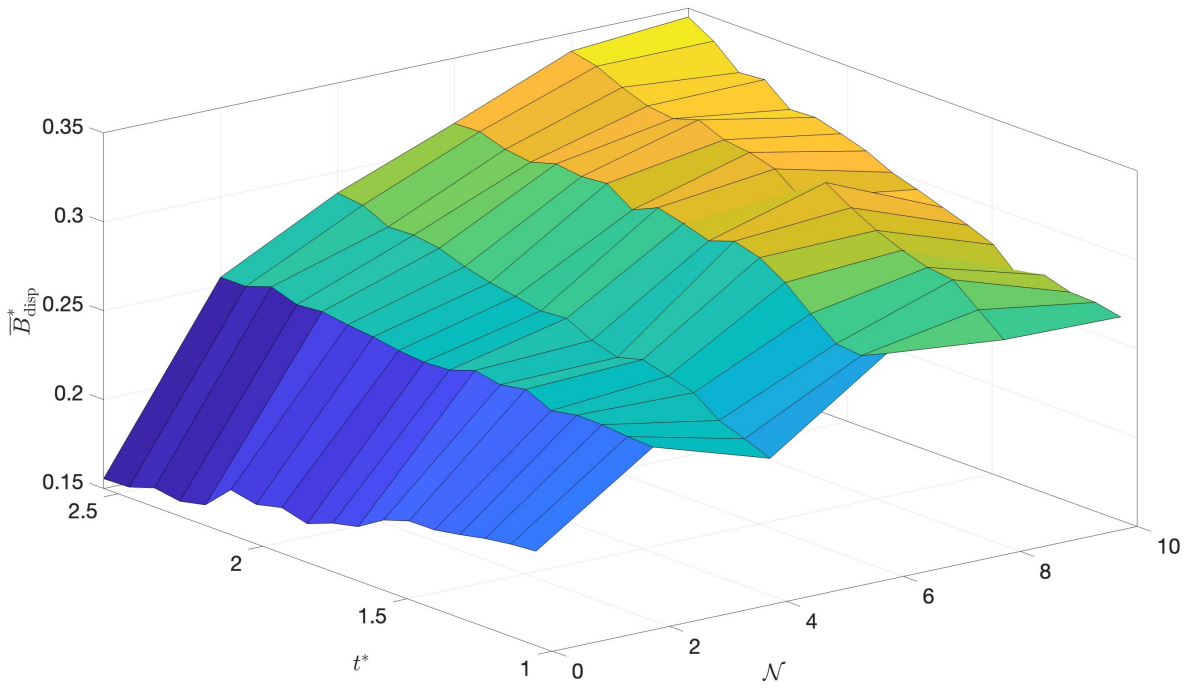

Figure 9: Dispersed buoyancy fraction vs. time and $\mathcal{N}$. Here we consider the same set of experiments from figures 5, 7 and 8.

with t^* but the trend is reversed when drainage is eliminated such that $\mathcal{N} = 0$. Note, however, that estimates of $\overline{B}^*_{\mathrm{disp}}$ for $\mathcal{N} = 0$ and small t^* may suffer from a bias owing to the elimination, by cropping, of the region directly adjacent to the nozzle. In said region, most of the fluid discharged by the nozzle is expected to be of the bulk phase variety owing to the limited opportunity for mixing with the ambient. By discounting this amount of bulk fluid, it may be the case that estimates of $\overline{B}^*_{\mathrm{disp}}$ moderately over-predict the true value of the dispersed buoyancy fraction. As such, we propose a more robust way of characterizing the variation of $\overline{B}^*_{\mathrm{disp}}$ below – see e.g. figure 11 and the discussion thereof.

Unfortunately, knowledge of the time evolution of B^*_{j} and even A^*_{j} does not provide especially meaningful insights into the rate of frontal advance of the gravity current, whether this is measured with respect to the bulk or dispersed phases. For this reason, and with reference to the same canonical set of experiments considered in figures 5, 7, 8, and 9, figure 10 shows time-series plots of the gravity current nose positions. After an initial adjustment

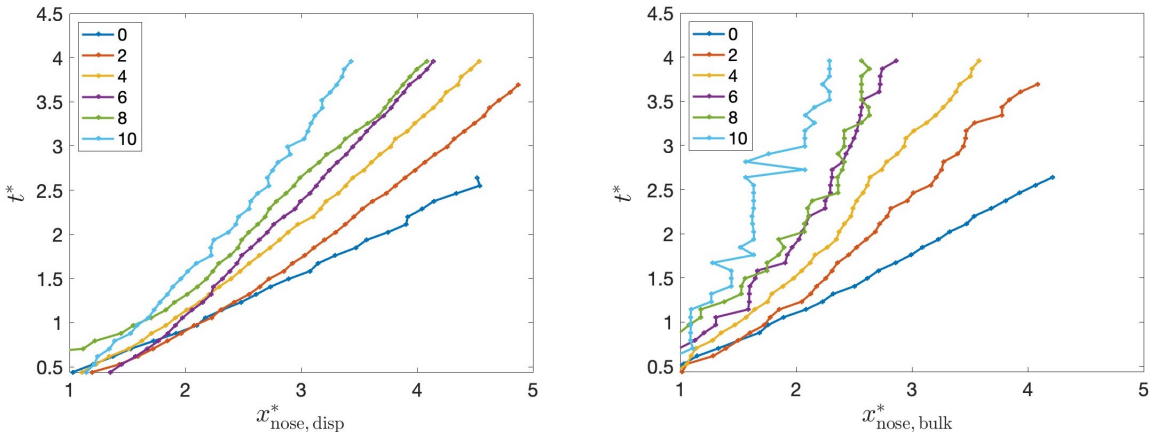

(a) (b)

Figure 10: Time evolution of the gravity current front as characterized by the (a) dispersed phase, $x^*_{\text{nose, disp}}$ and (b) bulk phase, $x^*_{\text{nose, bulk}}$. Here we consider the same set of experiments from figures 5, 7, 8 and 9. The greater scatter observed in (b) for large $\mathcal{N}$ is a consequence of the gravity current becoming very thin and therefore harder to visualize in experimental images – see e.g. figure 7.

phase, $x^*_{\text{nose, disp}}$ shows a roughly linear variation with time where the front speed decreases with increasing $\mathcal{N}$: as noted above, dispersion is fed by bulk fluid, which is disproportionately impacted by drainage. Consequently, when the amount of drainage increases, it becomes impossible for $x^*_{\text{nose, disp}}$ (or $x^*_{\text{nose, bulk}}$) to advance too quickly in the downstream direction. Indeed, the bulk phase data depicted in figure 10 b exhibit a greater sensitivity to $\mathcal{N}$ as evidenced by the fact that the associated time-series curves form a wider fan than is observed for the dispersed phase data of figure 10 a. When $\mathcal{N} = 8$ or 10 and t^* is large, the bulk phase is nearly arrested altogether. In these cases in particular, it seems doubtful that $x^*_{\text{nose, bulk}}$ will ever reach $x^* = 3$.

The results of figures 10 a,b suggest a different way of tracking the flow evolution of a particular experiment: rather than measuring e.g. $\overline{B}^*_{\text{disp}}$ against t^*, we can instead track the change of $\overline{B}^*_{\text{disp}}$ as $x^*_{\text{nose,disp}}$ reaches a fixed sequence of values. Such is the philosophy of figure 11, which replots the data of figure 9 but with the horizontal axis t^* replaced by $x^*_{\text{nose,disp}}$. In contrast to figure 9, the variation of $\overline{B}^*_{\text{disp}}$ is smoother than before. Partly, this is an artifact of the coarser resolution applied in figure 11. However, the regularization of

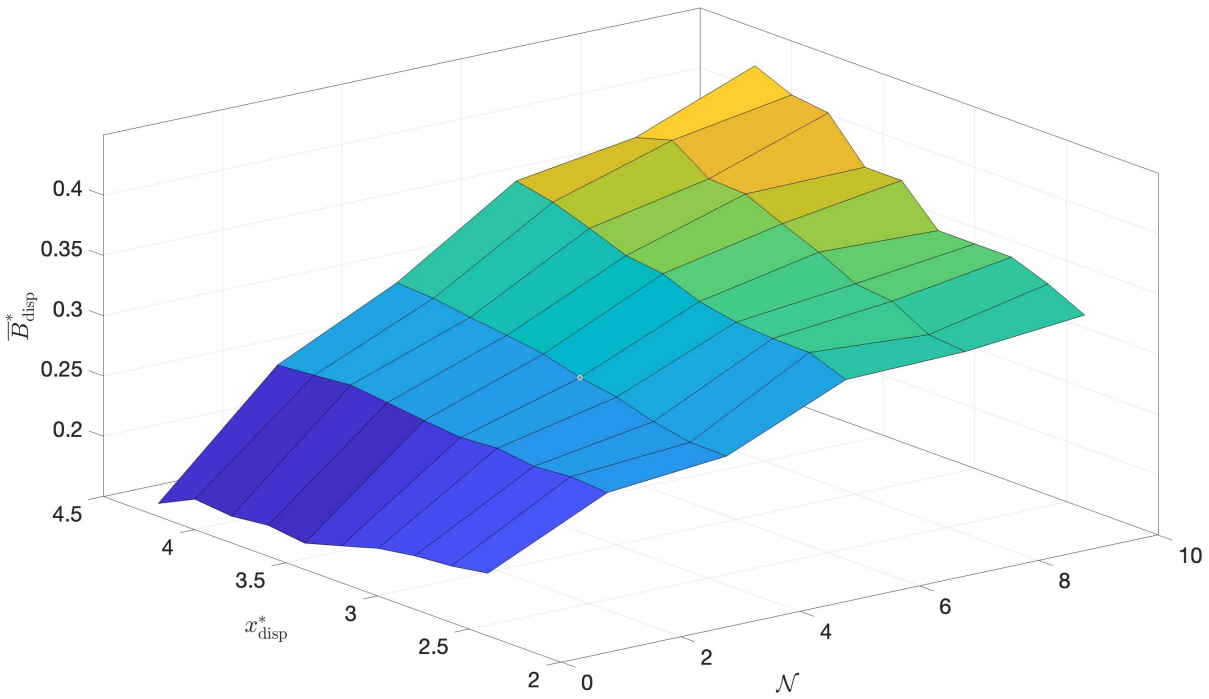

Figure 11: As in figure 9 but with $x^*_{\mathrm{nose,disp}}$ replacing t^* as one of the horizontal axes.

the surface for small values of $\mathcal{N}$ in particular suggests that frontal location rather than time may be the more meaningful metric when measuring the gravity current evolution. In any event, figure 11 reaffirms that $\overline{B}^*_{\mathrm{disp}}$ changes only by a moderate amount over the course of a typical experiment but that the dependence of $\overline{B}^*_{\mathrm{disp}}$ on $\mathcal{N}$ is more sensitive. Given this insight, we now consider the influence of other parameters, which we have deliberately held fixed in figures 5, 7, 8, 9, 10 and 11.

Figure 12 shows $\overline{B}^*_{\mathrm{disp}}$ vs. $\mathcal{N}$ for two different values of At and θ where the left- and right-hand side panels respectively consider $z^*_n = 0$ and $z^*_n > 0$. The top panels assume $\theta = 5°$ such that gravity current fluid flows down-dip whereas bottom panels assume $\theta = -5°$ such that gravity current fluid flows up-dip. Although all four panels of figure 12 consider the dispersed buoyancy fraction as the y-axis variable, marker sizes provide an indication of the total buoyancy present in both the bulk and dispersed phases. As expected, the makers having the largest diameters are therefore observed for the smallest $\mathcal{N}$, $\mathcal{N} = 0$ corresponding to the case of no fissure drainage.

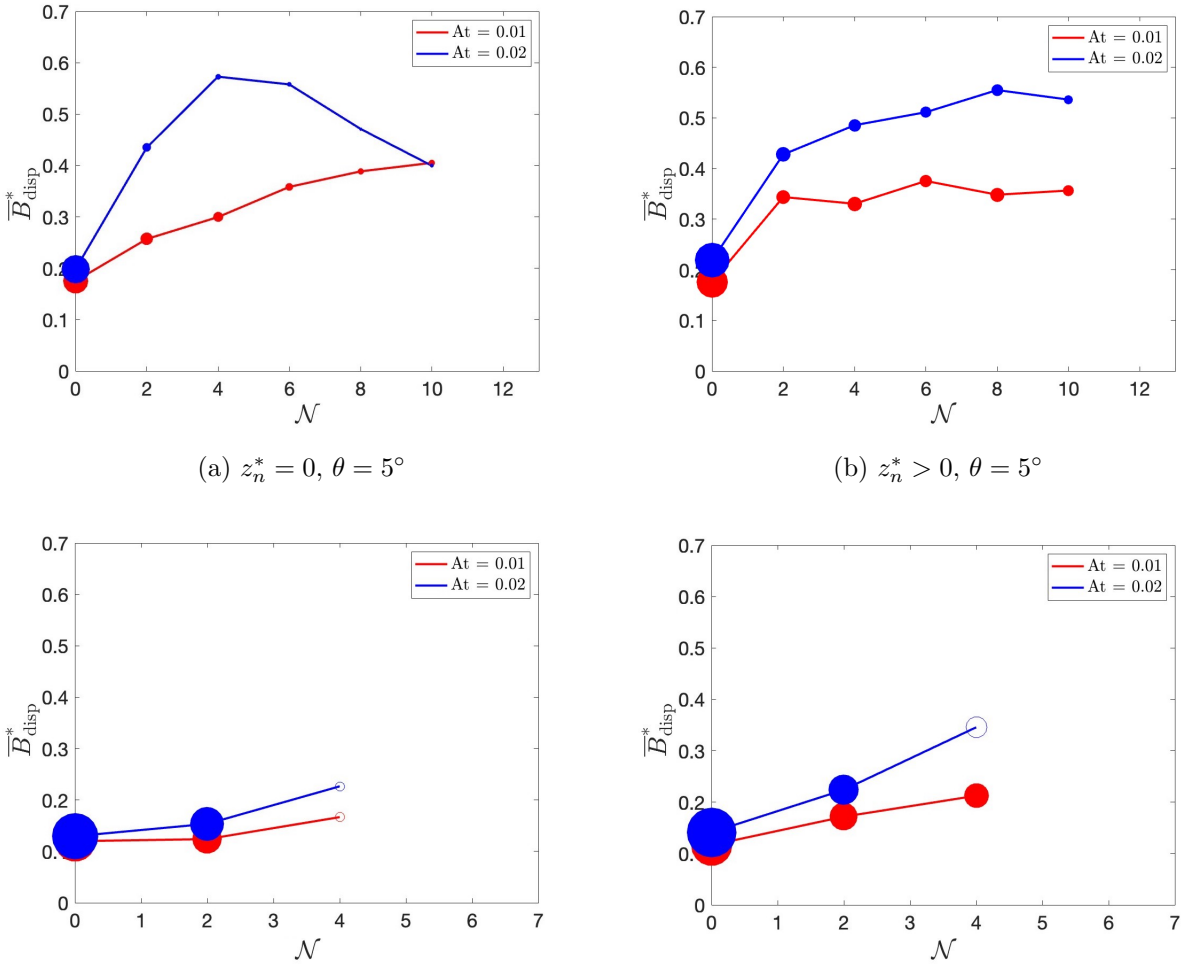

(a) $z_n^* = 0$, $\theta = 5°$

(b) $z_n^* > 0$, $\theta = 5°$

(c) $z_n^* = 0$, $\theta = -5°$

(d) $z_n^* > 0$, $\theta = -5°$

Figure 12: Dispersed buoyancy fraction vs. $\mathcal{N}$ for different At, θ and z_n^*. (In the case of an elevated nozzle, $z_n^* = 0.1469$ when At $= 0.02$ and $z_n^* = 0.1989$ when At $= 0.01$). Measurements of $\overline{B}^*_{\text{disp}}$ are made when $x^*_{\text{nose,disp}} = 4$. Marker diameters are proportional to the total buoyancy present within both of the bulk and dispersed phases. Open symbols signify that dispersed phase fluid does not extend to the downstream distance $x^* = 4$.

The red curve of figure 12a revisits the data from the back left edge of the surface from figure 11; accordingly, we observe a monotone increasing relationship between $\overline{B}^*_{\text{disp}}$ and $\mathcal{N}$. Doubling the value of At, i.e. shifting from the red curve to the blue curve has two important consequences. Firstly, and except at the limits $\mathcal{N} = 0$ or 10, the dispersed buoyancy fraction is notably larger for At $= 0.02$ than it is for At $= 0.01$: larger At is associated with larger

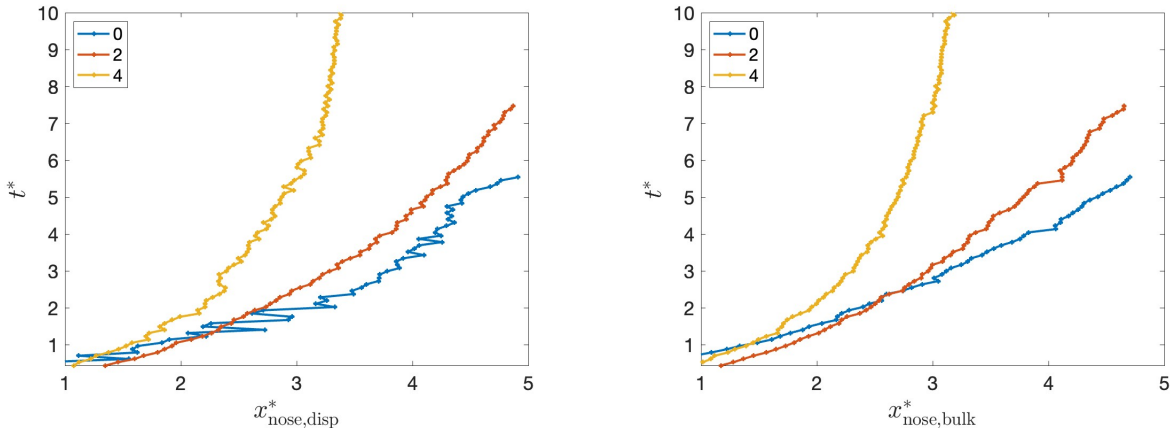

(a) (b)

Figure 13: As in figure 10 but for the up-dip flow experiments considered in figure 12c.

gravity current densities and therefore larger drainage velocities. In turn, more bulk fluid drains through the fissure when $\mathrm{At} = 0.02$, which has the effect of increasing $\overline{B}^*_{\text{disp}}$. Secondly, the blue curve exhibits an intriguing non-monotone variation with the number of open fissure holes such that $\overline{B}^*_{\text{disp}}$ decreases with $\mathcal{N}$ for $\mathcal{N} \gtrsim 5$. As can be inferred from figure 6, and for sufficiently large $\mathcal{N}$ and At, fissure drainage becomes so robust as to include not just bulk fluid but dispersed fluid also. The onset of such a state corresponds to a peak in the measured value of $\overline{B}^*_{\text{disp}}$.

Figure 12b considers the same parameters as figure 12a, but with an upward shift of nozzle elevation. The larger markers evident in Figure 12b vs. 12a suggest that fissure drainage is negatively impacted by raising the source and thereby diluting the dense fluid comprising the gravity current. Such dilution is a consequence of the entrainment of ambient fluid as source fluid forms a descending plume below the nozzle [25]. Thus, plume entrainment exerts a nuanced influence on the dispersed buoyancy fraction. On the one hand, plume entrainment, and its concomitant decrease of the drainage velocity, results in less bulk fluid loss through the fissure, which would otherwise decrease $\overline{B}^*_{\text{disp}}$. On the other hand, the mixing associated with plume entrainment yields an immediate supply of dispersed fluid, whose appearance and subsequent down-dip propagation would otherwise increase $\overline{B}^*_{\text{disp}}$. The precise impact of

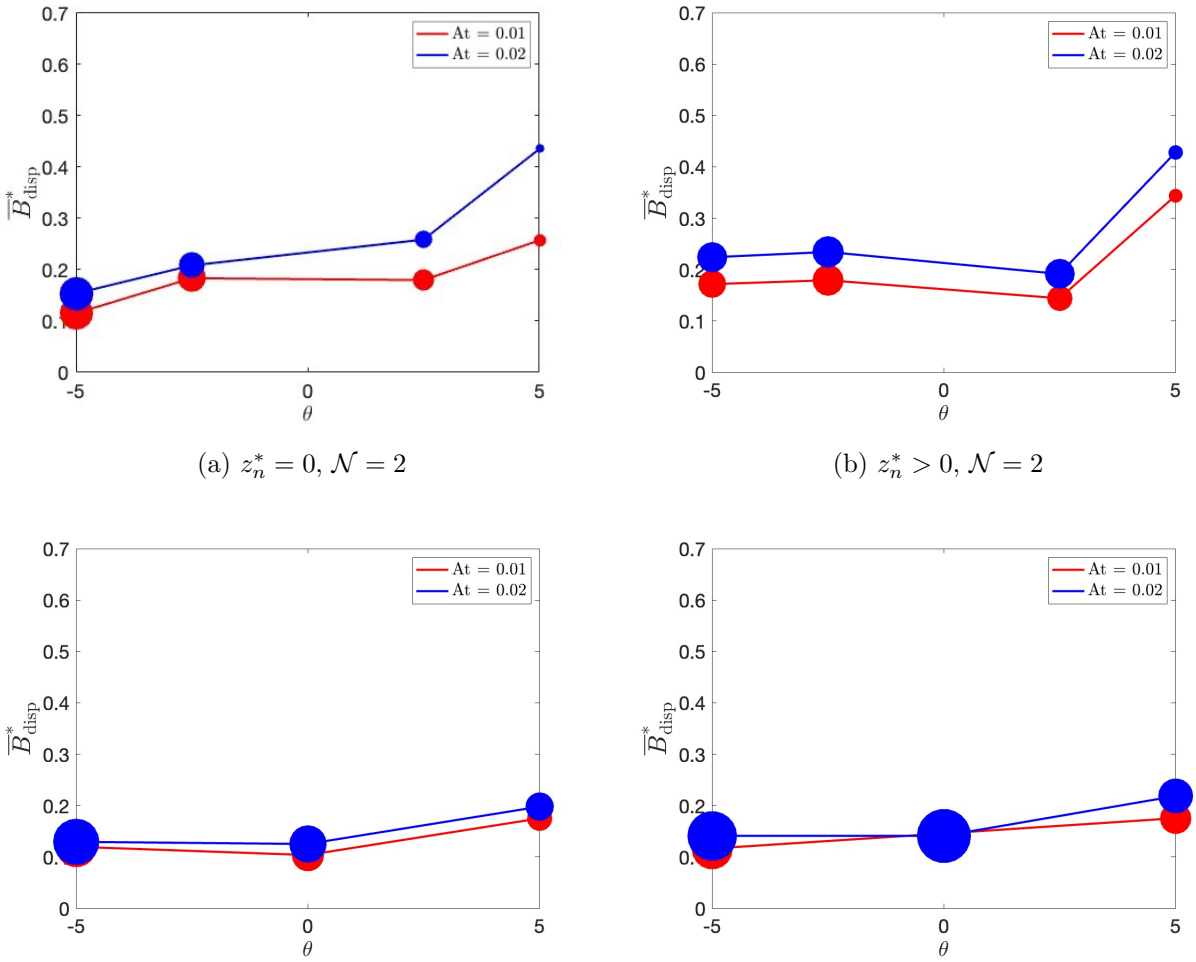

(a) $z_n^* = 0, \mathcal{N} = 2$

(b) $z_n^* > 0, \mathcal{N} = 2$

(c) $z_n^* = 0, \mathcal{N} = 0$

(d) $z_n^* > 0, \mathcal{N} = 0$

Figure 14: As in figure 12 but showing the variation of $\overline{B}^*_{\mathrm{disp}}$ with θ.

these counterbalancing effects is best appreciated by comparing the red and blue curves of figures 12a and 12b. When At $= 0.01$ and the nozzle is elevated, we observe that $\overline{B}^*_{\mathrm{disp}}$ does not steadily increase but rather saturates at approximately 0.35 for $\mathcal{N} > 2$. By contrast, and for At $= 0.02$, a raised nozzle causes $\overline{B}^*_{\mathrm{disp}}$ to achieve its maximum value (of approximately 0.55) when $\mathcal{N} = 8$, twice the critical $\mathcal{N}$ value associated with a non-raised nozzle.

Figures 12c and 12d present data analogous to figures 12a and 12b but for a different inclination angle, namely $\theta = -5°$. Here again, $\overline{B}^*_{\mathrm{disp}}$ generally increases with $\mathcal{N}$, albeit less aggressively than for down-dip flow. Correspondingly, $\overline{B}^*_{\mathrm{disp}}$ values for the $\theta = -5°$ cases are

Table 1: Dispersed buoyancy fractions as extracted from figures 14 a,c where $z_n^* = 0$. For comparison, the theoretical estimate derived from the model of Appendix B is also included. The percentage error is calculated via $(\overline{B}^*_{\rm disp,expt} - \overline{B}^*_{\rm disp,thy})/[\frac{1}{2}(\overline{B}^*_{\rm disp,expt} + \overline{B}^*_{\rm disp,thy})]$.

At	$\mathcal{N}$	θ (°)	$\overline{B}^*_{\rm disp,thy}$	$\overline{B}^*_{\rm disp,expt}$	% error
0.01	0	-5	0.101	0.120	17.2
		0	0.122	0.104	-15.9
		5	0.149	0.175	16.0
	2	-5	0.171	0.115	-39.2
		-2.5	0.189	0.183	-3.2
		2.5	0.203	0.180	-12.0
		5	0.221	0.257	15.1
0.02	0	-5	0.126	0.135	6.9
		0	0.164	0.130	-23.1
		5	0.206	0.198	-4.0
	2	-5	0.189	0.154	-20.4
		-2.5	0.213	0.208	-2.4
		2.5	0.257	0.258	0.4
		5	0.286	0.435	41.3

non-trivially smaller than those corresponding to $\theta = 5°$. By contrast, the time for flow and therefore total buoyancy retained in the porous medium is much larger when the gravity current flows up-dip – compare, for example, the marker diameters when $\mathcal{N} = 2$ in figures 12c and 12d vs. figures 12a and 12b. Also noteworthy is the difference of marker size when $\mathcal{N} = 4$ between figures 12c and 12d. This comparison confirms that much more buoyancy is retained in the porous medium when the nozzle is elevated, presumably because the plume entrainment that accompanies the raised source depresses drainage velocities. This has the effect of decreasing the volume of dense fluid discharged through the fissure, especially for larger $\mathcal{N}$.

Of course, increasing $\mathcal{N}$ carries the possibility that even the dispersed front will become

arrested before reaching the downstream location $x^* = 4$. Such cases are illustrated in figures 12c and 12d by the open symbols. So as to gain additional insights into the flow evolution for these experiments (plus their smaller $\mathcal{N}$ counterparts), we show in figure 13 the dispersed ($x^*_{\text{nose, disp}}$) and bulk ($x^*_{\text{nose, bulk}}$) nose positions vs. time. In all cases, At = 0.01. The yellow curves illustrate the $\mathcal{N} = 4$ case; as expected, the forward advance of both the dispersed and bulk fronts slows significantly as t^* increases. A less dramatic deceleration is noted when $\mathcal{N} = 2$ (orange curves) or, more especially, $\mathcal{N} = 0$ (blue curves). In these two cases, in particular, the dispersed layer remains comparatively thin.

Because figure 12 considers only two possible values for θ, i.e. $\theta = -5^\circ$ (up-dip flow) and $\theta = 5^\circ$ (down-dip flow), it is difficult to infer the precise impact of the inclination angle on $\overline{B}^*_{\text{disp}}$. Accordingly, each of the subplots of figure 14 fixes the values of $\mathcal{N}$ and the dimensional nozzle elevation but considers a more complete range of θ. Consistent with our previous remarks, $\overline{B}^*_{\text{disp}}$ generally increases with θ, however, figures 14a and 14b confirm that the variation can be decidedly nonlinear. These subplots further reveal that, as the inclination angle varies from $\theta = -5^\circ$ to $\theta = 5^\circ$ there is a corresponding decrease of marker size: when $\theta = 5^\circ$ such that the gravity current flows down-dip, advection speeds are large and the dispersed front reaches the downstream position $x^* = 4$ in much less time than is required when $\theta = -5^\circ$. Thus, there is much more opportunity for dense fluid to accumulate in the porous medium when the gravity current flows up-dip. This same trend is likewise evident when $\mathcal{N} = 0$ (bottom row of figure 14), although the decrease of marker size is less dramatic. In a similar spirit, the increase of $\overline{B}^*_{\text{disp}}$ as θ increases from -5° to 5° is comparatively minor: without draining and the disproportionate removal of bulk fluid, the fraction of bulk to dispersed fluid varies little with θ or, for that matter, At.

Taken together, figures 12 and 14 show that making adjustments to $\mathcal{N}$ and θ can cause $\bar{B}^*_{\text{disp}}$ to vary by almost half an order or magnitude. Though obviously nontrivial, this variety must be weighed against the much more substantial mixing that is possible in hetero- vs. homogeneous porous media. For instance, Sahu & Neufeld [26] performed experiments that explored gravity current flow through a porous medium characterized by discrete layers of different permeability. Using as their mixing metric the effective dispersive entrainment

coefficient, they concluded that "the amount of mixing in a heterogeneous medium can be higher by several orders of magnitude than that in a homogeneous medium depending on the type of heterogeneity." This substantial increase of mixing efficiency follows from the kind of motion observed by Sahu & Neufeld [26], i.e. their gravity currents first elongated through a layer of high permeability then experienced distributed drainage into a layer of low permeability. The resulting formation and elongation of convective fingers resulted in considerable mixing with the ambient fluid. In turn, the gravity current developed a blunt nose and lost its long, thin shape. By contrast, figures such as 5 and 6 confirm that the gravity currents of interest here become more, not less, slender over time. More importantly, we downplay the mixing directly associated with (discrete) basal draining focusing instead on the mixing that occurs along the upper (i.e. density-stable) surface of the gravity current. In this way, our results are, when inverted and extrapolated to real geophysical flows, reminiscent of buoyancy-driven flow along the underside of a caprock that is tight except for the appearance of a limited number of individual fissures.

7. Comparison with the theory of Sheikhi et al. (2023)

The comparisons drawn in figures 14 a,c can be extended in another direction, i.e. by contrasting measured results with fitted predictions derived from the theoretical model of Sheikhi et al. [29]. (A brief summary of Sheikhi et al.'s model appears in Appendix B. Because the model in question does not allow for non-zero z_n^*, no comparisons are possible with the data of figures 14 b,d.)

Theoretical estimates for $\overline{B}^*_{\text{disp}}$ are presented in table 1. Also included in this table are the experimental data from figures 14 a,c organized by At, $\mathcal{N}$ and θ. The error estimates that appear in the final column of table 1 quantify the difference between theoretical and experimental estimates of $\overline{B}^*_{\text{disp}}$ and include a roughly equal proportion of positive and negative values. Complementing the above discussion, figure 15 shows experimental snapshots from the $\mathcal{N} = 2$ experiments of table 1 where, in each case, $x^*_{\text{nose,disp}} = 4$. Panels (a) and (b) respectively consider At $= 0.01$ and At $= 0.02$ and the inclination angle is as indicated. In each sub-figure, we return to the white-red-yellow-blue-black color scheme adopted in

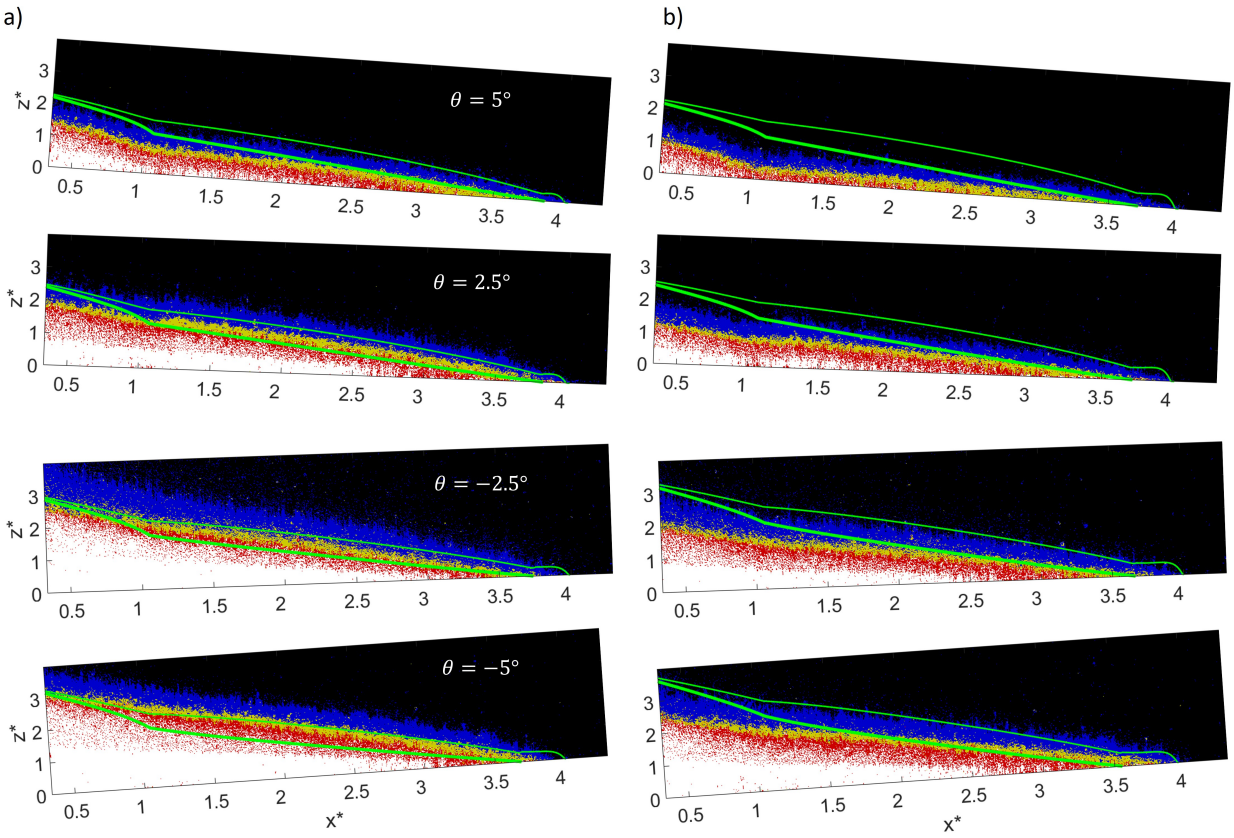

Figure 15: Gravity current profiles for various θ with $\mathcal{N} = 2$ and (a) At $= 0.01$, and, (b) At $= 0.02$. The white-red-yellow-blue-black color scheme is the same as defined in figure 5. In all cases, experimental snapshots correspond to a point in time where $x^*_{\text{nose,disp}} = 4$. Superimposed atop the experimental data are curves derived from the theoretical model of Appendix B. The thick (thin) green curve indicates the predicted profile of the bulk (dispersed) fluid.

figures 5, 6 and 7. Superimposed on the experimental snapshots are solid curves showing the theoretically-predicted profile for the bulk fluid (thick green curve) and the dispersed fluid (thin green curve). Ideal agreement would position the thick green curve along the red-yellow boundary and the thin green curves along the blue-black boundary and, indeed, such overlap is nearly realized in select cases e.g. At $= 0.01$, $\theta = 2.5°$, $x^* \gtrsim 1$ or At $= 0.02$, $\theta = -5°$, $x^* \gtrsim 1.5$. Elsewhere, greater discrepancies are observed, most especially when At $= 0.02$ and $\theta = 5°$.

Taken together, table 1 and figure 15 suggest that the theoretical model developed in

Sheikhi et al. [29] does only a fair job of predicting experimental trends. Consider, for example, the case At = 0.01, $\mathcal{N} = 2$ and $\theta = 2.5°$. Figure 15 a(ii) shows arguably the best agreement between theory and experiment of any of the panels for the figure in question. Even so, there is a -12.0% error between $\overline{B}^*_{\text{disp,thy}}$ and $\overline{B}^*_{\text{disp,expt}}$. By contrast, when At = 0.02, $\mathcal{N} = 2$ and $\theta = 2.5°$, $\overline{B}^*_{\text{disp,thy}}$ and $\overline{B}^*_{\text{disp,expt}}$ are in near perfect agreement and yet figure 15 b(ii) indicates that both the thick and thin green curves overestimate their respective boundaries. The observation concerning At = 0.01, $\mathcal{N} = 2$ and $\theta = 2.5°$ suggests that the theoretical model may over-estimate the degree the mixing by dispersion. More study is therefore recommended to determine whether the linear entrainment relationship developed in Sheikhi et al. [29], and adapted from investigations of analogue non-porous media flows, requires refinement. Meanwhile, the observation concerning At = 0.02, $\mathcal{N} = 2$ and $\theta = 2.5°$ suggests that the degree of fissure drainage may be insufficient, especially for higher gravity current densities. This implies that the fissure draining law quantified by (B.8), and derived from a generalization of Bernoulli's principle, may require modification for not small values of c_s.

A further persistent challenge for the theoretical model is to predict the correct profile heights upstream of the fissure at $x^* = 1$. This latter observation suggests that the theoretical model should be modified to allow for more dispersive mixing in the neighborhood of the gravity current source. The model presently requires the thick and thin green curves to merge in the limit $x^* \to 0$ but such an assumption is evidently not supported by the available experimental data.

8. Conclusions

Whereas dispersive mixing in porous media has attracted a great deal of attention, relatively few studies have explored dispersive mixing in the specific context of gravity current flow. Of particular interest is to couple dispersion and gravity current mass loss due to drainage. The current (experimental) work restricts drainage to an isolated fissure and therefore preserves the long and thin character of the gravity current. Doing so, and likewise examining a baseline case where the isolated fissure is closed altogether, allows us to

correlate drainage and dispersion and to explore the relationship between these two variables by leveraging the image processing algorithm described in section 4. Laboratory experiments are performed over a range of source densities (At), inclination angles (θ), fissure geometries ($\mathcal{N}$) and source elevations (z_n) and consider as a key metric the dispersed buoyancy fraction defined by (13). The dispersed buoyancy fraction measures the fraction of total buoyancy that resides in the dispersed phase and so serves as an effective measure of the degree of mixing between the gravity current and ambient.

On the basis of our experimental measurements, the following key findings follow:

- As fissure draining becomes more significant, so too does the relative importance of dispersion: draining preferentially removes so-called bulk fluid having a density close to that of the gravity current source, ρ_s. Thus, in comparative sense, the domain typically contains more dispersed fluid, whose density falls closer to the ambient density, $\rho_a < \rho_s$.

- The effect just described becomes more prevalent at larger ρ_s (i.e. larger At) because of the corresponding increase of the drainage velocity. Generally similar comments apply to the number, $\mathcal{N}$, of discrete openings comprising the isolated fissure. Indeed, for sufficiently large $\mathcal{N}$, we find that the gravity current becomes arrested such that its volume and buoyancy both plateau.

- When the (dense) gravity current is fed by an elevated source such that a descending plume forms, the amount of dispersive mixing experienced upstream of the fissure increases. As a consequence, however, fissure drainage is depressed. Thus the dispersed buoyancy fraction or $\overline{B}^*_{\text{disp}}$ tends to an asymptotic value in the limit of large $\mathcal{N}$ – see e.g. figure 12 b.

- Forcing the gravity current to propagate up-dip causes the flow to arrest earlier and even causes the dispersed phase to reach a terminal "run-out" length. Because of the limited opportunity for dispersive mixing when the up-dip inclination angle is sufficiently large, the volume of dispersed fluid realized for large negative θ is much smaller than what is realized for large positive θ. On the other hand, for $\theta = -2.5°$,

$\theta = 0°$ and even $\theta = 2.5°$, figure 14 confirms that the degree of dispersion is often comparable to that measured at $\theta = -5°$.

Although we have avoided extrapolating our results to real UHS systems, which present many more complications than are considered in our idealized experiments, it is worth considering the significance of this last finding. In particular, provided structural trapping in the form of an anticline is available, the degree of dispersion is predicted to be approximately independent of dip angle. Of course, more steeply-sloped anticlines may offer other advantages relative to their shallow-sloped counterparts e.g. hydrogen will ultimately collect in a deeper layer such that, during the production phase, the likelihood of coning (i.e. the co-extraction of hydrogen and cushion gas) is minimized.

In drawing comparisons between measured results and the analogue theory previously published by Sheikhi et al. [29], table 1 shows fair agreement between experimental and theoretical estimates of $\overline{B}^*_{\mathrm{disp}}$. The ability of the theory to correctly anticipate the gravity current profile (including the shape of the bulk and dispersed phases) is likewise nuanced as figure 15 confirms. Whereas generally good agreement is seen at large x^* and small At and θ, the model significantly over-predicts the height of both phases when At and θ are large. One possible contributor to this discrepancy is that the model assumes very limited mixing in the neighborhood of the source, an assumption that ought to be relaxed in further iterations of the theory.

Other ideas for future work include adding multiple isolated fissures or including some degree of heterogeneity within the porous medium itself. Whereas the experiments in question could be performed by a straightforward modification of the set-up of section 2.1, there remain other important topics for investigation that would necessitate a more elaborate experimental redesign. For instance, the flows we consider are nominally 2-D rectilinear. However, and given that the motivation for this study derives from the seasonal storage of hydrogen in depleted natural gas reservoirs, it would be helpful to consider more complicated flow patterns e.g. 2-D axisymmetric or fully 3-D. In this latter case, in particular, it would be important to characterize the role of dispersion in the transverse direction. By

design, transverse dispersion is ignored here, however, its impact at the large spatial scales that characterize real UHS flows is, almost certainly, important. By extension, we do not expect the results of e.g. figure 14 to be quantitatively accurate when transverse dispersion results in significant (i.e. non-local) variations in the pattern of gravity current spread.

Also critical to explore in the UHS context is the impact of a transient source that discharges, then later aspirates, gravity current fluid having a different density and viscosity than the fluid saturating the porous medium. For such a scenario, the evolution of the gravity current and, more especially, the dispersed phase, has yet to be fully characterized. Such a characterization is essential to an evaluation of the feasibility, commercial and otherwise, of field-scale hydrogen storage projects.

Author contributions, conflict of interest and funding acknowledgment

MS performed the experiments and post-processed the experimental images, with detailed technical assistance from KSB. SS developed the theoretical model and generated the theoretical data that appears, for example, in table 1. MRF supervised the work and co-wrote the manuscript with MS. All four authors declare that they have no conflict of interest. Funding for this project was generously provided by NSERC through the Discovery Grant and USRA programs.

Appendix A. List of experiments

A detailed list summarizing all of the laboratory experiments conducted over the course of this study is provided in tabular format below.

Table A.2: Experimental parameters, organized by experiment identifier (Expt. ID). Here, θ refers to the tank inclination angle, $\mathcal{N}$ refers to the number of open fissure holes, At refers to the Atwood number (defined by equation 6), z_n^* refers to the non-dimensional nozzle elevation and 'Duration' refers to the non-dimensional time needed for $x^*_{\text{nose,disp}} = 4x_f$. A dash in the final column signifies that the dispersed phase became arrested before $x^*_{\text{nose,disp}}$ reached $4x_f$.

Expt. ID	θ (°)	$\mathcal{N}$	At	$z_n^* = z_n/H$	Duration
E1	5	0	0.01	0	2.1
E2	5	0	0.02	0	2.4
E3	5	0	0.01	0.1989	2.4
E4	5	0	0.02	0.1469	2.6
E5	5	2	0.01	0	2.6
E6	5	2	0.02	0	2.9
E7	5	2	0.01	0.1989	3.0
E8	5	2	0.02	0.1469	2.9
E9	5	4	0.01	0	3.2
E10	5	4	0.02	0	3.7
E11	5	4	0.01	0.1989	3.5
E12	5	4	0.02	0.1469	3.7
E13	5	6	0.01	0	3.9
E14	5	6	0.02	0	4.0
E15	5	6	0.01	0.1989	3.7
E16	5	6	0.02	0.1469	4.2
E17	5	8	0.01	0	4.0
E18	5	8	0.02	0	4.3
E19	5	8	0.01	0.1989	3.7
E20	5	8	0.02	0.1469	4.4
E21	5	10	0.01	0	4.2
E22	5	10	0.02	0	4.4

Continued on next page

Table A.2 – continued from previous page

Expt. ID	θ (°)	$\mathcal{N}$	At	$z_n^* = z_n/H$	Duration
E23	5	10	0.01	0.1989	3.7
E24	5	10	0.02	0.1469	5.1
E25	2.5	2	0.01	0	2.8
E26	2.5	2	0.02	0	3.3
E27	2.5	2	0.01	0.1989	3.2
E28	2.5	2	0.02	0.1469	3.3
E29	0	0	0.01	0	3.0
E30	0	0	0.02	0	3.2
E31	0	0	0.01	0.1989	2.6
E32	0	0	0.02	0.1469	4.2
E33	-2.5	2	0.01	0	3.9
E34	-2.5	2	0.02	0	4.8
E35	-2.5	2	0.01	0.1989	3.8
E36	-2.5	2	0.02	0.1469	4.3
E37	-5	0	0.01	0	3.3
E38	-5	0	0.02	0	3.9
E39	-5	0	0.01	0.1989	3.5
E40	-5	0	0.02	0.1469	4.3
E41	-5	2	0.01	0	4.4
E42	-5	2	0.02	0	6.3
E43	-5	2	0.01	0.1989	5.9
E44	-5	2	0.02	0.1469	7.4
E45	-5	4	0.01	0	14.3
E46	-5	4	0.02	0	-
E47	-5	4	0.01	0.1989	7.6

Continued on next page

Table A.2 – continued from previous page

Expt. ID	θ (°)	$\mathcal{N}$	At	$z_n^* = z_n/H$	Duration
E48	-5	4	0.02	0.1469	-

Appendix B. Theoretical model summary

A comprehensive derivation of the theoretical model is presented in Sheikhi et al. [29]; only a brief review is provided here.

We assume a two-dimensional gravity current flow as depicted schematically in figure 2 where the bulk (density ρ_s, height h_{bulk}), dispersed (density ρ_{disp}, height $h_{\text{disp}} - h_{\text{bulk}}$) and ambient (density ρ_a) phases are all miscible (and incompressible). With reference to the coordinate system indicated in figure 2, mass continuity as applied to the bulk phase requires that

$$\phi \frac{\partial h_{\text{bulk}}}{\partial t} + \frac{\partial}{\partial x}(u_{\text{bulk}} h_{\text{bulk}}) = -w_{e1} - w_d\, F(x, x_f, \xi)\,, \tag{B.1}$$

where ξ is the width of the (line) fissure and $F(x, \xi)$ is a boxcar function centered on this fissure. In (B.1), reference is made to three Darcy velocities; u_{bulk} is the z-independent speed of the bulk phase, w_d accounts for fissure drainage and w_{e1} accounts for entrainment from the bulk to the dispersed phase. For simplicity, we assume a linear entrainment relationship such that $w_{e1} = \epsilon u_{\text{bulk}}$ where ϵ is an entrainment coefficient. In the dispersed phase, meanwhile, mass considerations yield

$$\phi \frac{\partial (h_{\text{disp}} - h_{\text{bulk}})}{\partial t} + \frac{\partial}{\partial x} \int_{h_{\text{bulk}}}^{h_{\text{disp}}} u_{\text{disp}} \mathrm{d}z = w_{e1} + w_{e2}\,. \tag{B.2}$$

Here, $u_{\text{disp}} \neq u_{\text{bulk}}$ is the speed of the dispersed phase and $w_{e2} = \epsilon u_{\text{disp}}$ accounts for entrainment from the ambient to the dispersed phase. Application of (B.1) in (B.2) shows that

$$\phi \frac{\partial h_{\text{disp}}}{\partial t} + \frac{\partial}{\partial x}\big[u_{\text{disp}}(h_{\text{disp}} - h_{\text{bulk}})\big] = -\frac{\partial}{\partial x}(u_{\text{bulk}} h_{\text{bulk}}) + w_{e2} - w_d\, F(x, x_f, \xi)\,. \tag{B.3}$$

Whereas the solute concentration in the bulk phase, c_s, matches that of the source, the solute concentration, c_{disp}, in the dispersed phase must be computed from the following

conservation equation:

$$\phi\frac{\partial}{\partial t}\int_{h_{\rm bulk}}^{h_{\rm disp}} c_{\rm disp}\mathrm{d}z + \frac{\partial}{\partial x}\int_{h_{\rm bulk}}^{h_{\rm disp}} u_{\rm disp}c_{\rm disp}\mathrm{d}z = w_{e1}c_s\,. \tag{B.4}$$

This last result can be simplified to

$$\phi\frac{\partial b_{\rm disp}}{\partial t} + \frac{\partial}{\partial x}(u_{\rm disp}b_{\rm disp}) = w_{e1}c_s \tag{B.5}$$

by defining $b_{\rm disp} = \overline{c}_{\rm disp}(h_{\rm disp} - h_{\rm bulk})$ where $\overline{c}_{\rm disp}$ is the z-averaged solute concentration in the dispersed phase.

Equations (B.1), (B.3) and (B.5) can be solved for $h_{\rm bulk}$, $h_{\rm disp}$ and $b_{\rm disp}$ provided expressions are available for the Darcy velocities $u_{\rm bulk}$, $u_{\rm disp}$ and w_d. The expressions in question derive from Darcy's law where we assume (i) a hydrostatic pressure gradient, and, (b) a linear equation of state. To wit, it can be shown that

$$u_{\rm bulk}(x,t) = -\frac{kg\beta}{\nu}\Big[\frac{\partial b_{\rm disp}}{\partial x}\cos\theta + c_s\Big(\frac{\partial h_{\rm bulk}}{\partial x}\cos\theta - \sin\theta\Big)\Big]\,, \tag{B.6}$$

$$u_{\rm disp}(x,t) = -\frac{kg\beta}{\nu}\Big[\frac{\partial}{\partial x}\Big(\frac{b_{\rm disp}h_{\rm disp}}{h_{\rm disp} - h_{\rm bulk}}\Big)\cos\theta - \frac{b_{\rm disp}}{h_{\rm disp} - h_{\rm bulk}}\sin\theta\Big]\,, \tag{B.7}$$

and

$$w_d(x,t) = \frac{k_f g\beta}{\nu}\Big(\frac{c_s h_{\rm bulk} + b_{\rm disp}}{l} + c_s\Big)\cos\theta\,. \tag{B.8}$$

Here, g is gravitational acceleration, β is the solute contraction coefficient and ν is the kinematic viscosity. Meanwhile k_f and l are the permeability and depth of the fissure.

Important to acknowledge in the context of table 1 is that the k_f of (B.8) is used as a fitting parameter and is chosen to minimize the overall error between $\overline{B}^*_{\rm disp,thy}$ and $\overline{B}^*_{\rm disp,expt}$. Thus do we select $k_f = 5.0k$ when At $= 0.01$ and $k_f = 2.5k$ when At $= 0.02$. The justification for making k_f a function of At comes from figure 7 of Roes et al. [24], which confirms that, similar to the discharge coefficients for tank flow, fissure permeabilities depend on the density of the discharging fluid. The mechanistic rationalization comes from the study of Holford & Hunt [16], who surmised that density effects may cause a contraction of the discharging flow over and above that associated with inertia. In this respect, note that (i) not dissimilar observations have been made in the context of porous media flow, i.e. Bolster et al. [4]

ascertained that the effective permeability of a heterogeneous medium may be influenced by the fluid density, and, (ii) fitting the value of k_f allows us to apply a purely rectilinear theoretical model to experimental data in which fissure drainage occurs via a series of up to $\mathcal{N} = 10$ discrete circular openings.

References

[1] Amid, A., Mignard, D., Wilkinson, M., 2016. Seasonal storage of hydrogen in a depleted natural gas rsservoir. Intl. J. Hydrogen Energy 41, 5549–5558.

[2] Bharath, K., Sahu, C.K., Flynn, M.R., 2020. Isolated buoyant convection in a two-layered porous medium with an inclined permeability jump. J. Fluid Mech. 902, A22.

[3] Blunt, M.J., Bazylak, A., Brook, M., Muggeridge, A., Orr Jr., F.M., 2024. Research needs in porous media for the energy transition. InterPore Journal 1, 1–12.

[4] Bolster, D.T., Neuweiler, I., Dentz, M., Carrera, J., 2011. The impact of buoyancy on front spreading in heterogeneous porous media in two-phase immiscible flow. Water Resources Res. 47.

[5] Carden, P.O., Paterson, L., 1979. Physical, chemical and energy aspects of underground hydrogen storage. Intl. J. Hydrogen Energy 4, 559–569.

[6] Dong, W., Salvadurai, A.P.S., 2006. Image processing technique for determining the concentration of a chemical in a fluid-saturated porous medium. Geotech. Testing J. 29, 385–391.

[7] Dullien, F., 1979. 1979 Porous Media: Fluid Transport and Pore Structure. Academic Press, Inc.

[8] Dunn, S., 2002. Hydrogen futures: Toward a sustainable energy system. Intl. J. Hydrogen Energy 27, 235–264.

[9] Feldmann, F., Hagemann, B., Ganzer, L., Panfilov, M., 2016. Numerical simulation of hydrodynamic and gas mixing processes in underground hydrogen storages. Environ. Earth Sci. 75, 1165.

[10] Hagemann, B., Panfilov, M., Ganzer, L., 2016. Multicomponent gas rising through water with dissolution in stratified porous reservoirs – Application to underground storage of H_2 and CO_2. J. Natural Gas Sci. Engg. 31, 198–213.

[11] Happel, J., Brenner, H., 1983. Low Reynolds Number Hydrodynamics. Martinus Nijhoff Publishers.

[12] Hassanpouryouzband, A., Joonaki, E., Edlemann, K., Haszeldine, R.S., 2021. Offshore geological storage of hydrogen: Is this our best option to achieve net-zero? ACS Energy Lett. 6, 2181–2186.

[13] Hauck, T.E., 2021. Salt stratigraphy: Salt caverns in the Elk Point Group of Alberta, in: GeoConvention2021.

[14] Heinemann, N., co authors, 2021. Enabling large-scale hydrogen storage in porous media – the scientific challenges. Energy Environ. Sci. 14, 853–864.

[15] Hematpur, H., Abdollahi, R., Rostami, S., Haghighi, M., Blunt, M.J., 2023. Review of underground hydrogen storage: Concepts and challenges. Advances in Geo-Energy Research 7, 111–131.

[16] Holford, J.M., Hunt, G.R., 2001. The dependence of the discharge coefficient on denity contrast – Experimental measurements, in: Proc. 14th Australian Fluid Mechanics Conf., Adelaide Univ., pp. 123–126.

[17] Huppert, H.E., Neufeld, J.A., Strandkvist, S., 2013. The competition between gravity and flow focusing in two-layered porous media. J. Fluid Mech. 720, 5–14.

[18] Masoudi, M., Hassanpouryouzband, A., Hellevang, H., Haszeldine, R.S., 2024. Lined rock caverns: A hydrogen storage solution. J. Energy Storage 84, 110927.

[19] Muhammed, N.S., co authors, 2023. Hydrogen storage in depleted gas reservoirs: A comprehensive review. Fuel 337, 127032.

[20] Muhammed, N.S., Haq, B., Shehri, D.A., Al-Ahmed, A., Rahman, M.M., Zaman, E., 2022. A review on underground hydrogen storage: Insight into geological sites, influencing factors and future outlook. Energy Rep. 8, 461–499.

[21] Neufeld, J., Vella, D., Huppert, H., 2009. The effect of a fissure on storage in a porous medium. Journal of Fluid Mechanics 639, 239–259.

[22] Ozarslan, A., 2012. Large-scale hydrogen energy storage in salt caverns. Intl. J. Hydrogen Energy 37, 14265–14277.

[23] Roes, M.A., 2014. Buoyancy-driven convection in a ventilated porous medium. Master's thesis. University of Alberta.

[24] Roes, M.A., Bolster, D.T., Flynn, M.R., 2014. Buoyant convection from a discrete source in a leaky porous medium. J. Fluid Mech. 755, 204–229.

[25] Sahu, C.K., Flynn, M.R., 2015. Filling box flows in porous media. J. Fluid Mech. 782, 455–478.

[26] Sahu, C.K., Neufeld, J.A., 2023. Experimental insights into gravity-driven flows and mixing in layered porous media. J. Fluid Mech. 956, A27.

[27] Sainz-Garcia, A., Abarca, E., Rubi, V., Grandia, F., 2017. Assessment of feasible strategies for seasonal underground hydrogen storage in a saline aquifer. International Journal of Hydrogen Energy 42, 16657–16666.

[28] Sheikhi, S., Flynn, M.R., 2024. Porous media gravity current flow over an interbed layer: the impact of dispersion and distributed drainage. J. Fluid Mech. 984, A33.

[29] Sheikhi, S., Sahu, C., Flynn, M.R., 2023. Dispersion effects in porous media gravity currents experiencing local drainage. J. Fluid Mech. 975, A18.

[30] Tarkowski, R., 2019. Underground hydrogen storage: Characteristics and prospects. Renewable and Sustainable Energy Reviews 105, 86–94.

[31] Zhang, X., Zhao, X., Smith, S., Xu, J., Yu, X., 2016. Hydrogen production from renewable energy sources: Current status, technological advances, and future directions. Renewable and Sustainable Energy Reviews 69, 793–821. doi:10.1016/j.rser.2016.11.100.